Planetary and Space Science 61 (2012) 15–31

Contents lists available at SciVerse ScienceDirect

Planetary and Space Science

journal homepage: www.elsevier.com/locate/pss

Influence of upstream solar wind on thermospheric flows at Jupiter

J.N. Yates [a,b,*], N. Achilleos [a,b], P. Guio [a,b]

[a] Department of Physics and Astronomy, University College London, Gower Street, London, UK
[b] Centre for Planetary Sciences at UCL/Birkbeck, University College London, Gower Street, London, UK

ARTICLE INFO

Article history:
Received 15 December 2010
Received in revised form
12 August 2011
Accepted 19 August 2011
Available online 6 September 2011

Keywords:
Jupiter
Magnetosphere
Thermosphere
Ionosphere
Aurora

ABSTRACT

The coupling of Jupiter's magnetosphere and ionosphere plays a vital role in creating its auroral emissions. The strength of these emissions is dependent on the difference in speed of the rotational flows within Jupiter's high-latitude thermosphere and the planet's magnetodisc. Using an azimuthally symmetric global circulation model, we have simulated how upstream solar wind conditions affect the energy and direction of atmospheric flows. In order to simulate the effect of a varying dynamic pressure in the upstream solar wind, we calculated three magnetic field profiles representing compressed, averaged and expanded 'middle' magnetospheres. These profiles were then used to solve for the angular velocity of plasma in the magnetosphere. This angular velocity determines the strength of currents flowing between the ionosphere and magnetosphere. We examine the influence of variability in this current system upon the global winds and energy inputs within the Jovian thermosphere. We find that the power dissipated by Joule heating and ion drag increases by $\sim 190\%$ and $\sim 185\%$ from our compressed to expanded model respectively. We investigated the effect of exterior boundary conditions on our models and found that by reducing the radial current at the outer edge of the magnetodisc, we also limit the thermosphere's ability to transmit angular momentum to this region.

1. Introduction

Amongst the eight planets in the solar system, Jupiter, in addition to being the largest planet, also has the largest magnetic moment and the largest magnetosphere. The magnetosphere interacts with both the solar wind and the conducting layer or ionosphere, in the planet's upper atmosphere. These interactions can be quite complex and we may use models with some simplifying assumptions (e.g. axial symmetry) to gain insight into the dynamics of the magnetosphere, upper atmosphere and their physical interactions with the solar wind.

Several models of Jupiter's magnetosphere and ionosphere have been developed in recent studies (Nichols and Cowley, 2004; Cowley et al., 2005, 2007; Smith and Aylward, 2009). These models range from detailed studies of the middle magnetosphere only (Nichols and Cowley, 2004) to global studies of the entire magnetosphere (Cowley et al., 2005, 2007) and investigations of the coupled magnetosphere, thermosphere and ionosphere systems (Smith and Aylward, 2009) (henceforth SA09).

One of the important observations for guiding models is the dominance of Jupiter's magnetosphere by the rapid planetary rotation. Angular momentum is transferred from the planet to the disc-like middle magnetosphere via ion-neutral collisions in the ionosphere. The magnetospheric plasma exhibits a wide range of angular velocities, corresponding to a modest departure from rigid corotation with the planet at distances near Io (6–10 R_J) out to regions beyond 20 R_J which rotate at $\sim 50\%$ of the planetary rate (McNutt et al., 1979; Hill, 1979; Hill et al., 1983a; Pontius, 1997; Vasyliunas, 1983). This angular momentum and energy transfer between the ionosphere and magnetosphere are conveyed by two principal current systems. The first of these is related to the rotation of the middle magnetosphere. The second is related to the interaction of the solar wind with the magnetosphere at the high-latitude magnetopause (Hill et al., 1983b; Isbell et al., 1984).

The principal source of plasma for the middle magnetosphere (from ~ 20 R_J to several tens of R_J) is the satellite Io (Bagenal and Sullivan, 1981) which ejects about 500–1000 kg s^{-1} of sulphur dioxide gas which is then ionised (Kivelson et al., 2004). Iogenic plasma initially near corotation will lag further behind corotation as it diffuses radially outwards from the Io torus, due to the finitely conducting ionosphere being unable to supply all of the necessary angular momentum via the coupling currents. The electric field in the neutral atmosphere's rest frame depends on the difference in angular velocity between the polar thermosphere and the magnetically conjugate plasma disc, and drives a flow of equatorially directed Pedersen currents. Due to current continuity, field-aligned current (FAC) in the steady-state must

* Corresponding author at: Department of Physics and Astronomy, University College London, Gower Street, London, UK. Tel.: +44 20 7679 4349; fax: +44 20 7679 2328.
E-mail address: japheth@star.ucl.ac.uk (J.N. Yates).

0032-0633/$ - see front matter © 2011 Elsevier Ltd. All rights reserved.
doi:10.1016/j.pss.2011.08.007

flow both upwards and downwards along the magnetic field lines which connect the ionosphere and magnetospheric plasma disc. Downward FACs flow from the outermost magnetosphere to the ionosphere. The upward directed FACs are carried by downward precipitating electrons from the magnetosphere (Cowley and Bunce, 2001; Hill, 2001; Khurana, 2001; Southwood and Kivelson, 2001). These electrons excite emissions in the upper atmosphere and produce the main auroral oval at $\sim 15^{\circ}$ co-latitude (Satoh et al., 1996; Clarke et al., 1998, 2004; Prangé et al., 1998; Vasavada et al., 1999; Pallier and Prangé, 2001; Grodent et al., 2003). Currents flow radially outward in the equatorial plane of the magnetosphere and, via the $\boldsymbol{J} \times \boldsymbol{B}$ force, accelerate the plasma towards corotation. The Pedersen, radial and FACs thus represent a complete current 'circuit' coupling the magnetosphere and ionosphere.

The thermospheric angular velocity at Jupiter partly controls the ionospheric Pedersen currents and thus the dynamics of the magnetosphere. We do not, however, have many measurements of these thermospheric velocities. Studies such as Huang and Hill (1989) and Pontius (1995) have attempted to model these velocities by coupling the magnetosphere, ionosphere and thermosphere, with the assumption that angular momentum was transported through the thermosphere solely by vertical viscous transport. These studies yielded two main conclusions: (i) the relationship between thermospheric and magnetospheric angular velocities was a linear one and (ii) thermospheric dynamics could be parameterised using an 'effective' ionospheric conductivity, which represented the effects of the difference in angular velocity of the thermosphere and deep atmosphere (i.e. planetary value).

Smith and Aylward (2008) and SA09 showed that, for both Saturn and Jupiter, meridional advection rather than vertical viscous transfer is the main process by which angular momentum is distributed to the high latitude thermosphere. They also showed that the neutral atmosphere super-corotates, ultimately due to the sub-corotation of the middle and outer magnetosphere, at latitudes just equatorwards of the boundary between the field lines of the middle magnetosphere and the Dungey–Vasyliunas (D–V) layer (region II in Section 3.1.1). Super-corotation occurs in a region where ion drag forces (promote sub-corotation) are insignificant compared to Coriolis forces (promote corotation). These regions, where ion drag tends to zero, lead to the upwelling of gas which expands and cools adiabatically. This then causes a pressure gradient which drives poleward flows at altitudes less than 600 km (pressures higher than 0.04 μbar). As ion drag is insignificant in this region, the Coriolis force has no obstruction and can accelerate the gas to super-corotate. 'Hotspots' were created in these models by converging meridional winds at the poles while lower latitude regions were cooled. For more detailed conclusions the reader is referred to SA09.

The modelling of SA09 combined the advanced middle magnetosphere model of Nichols and Cowley (2004) with the axisymmetric model of the entire magnetosphere presented in Cowley et al. (2005). These magnetospheric inputs were then coupled to a global two-dimensional circulation model of the Jovian thermosphere. The auroral region in this coupled model is represented by the one-dimensional auroral thermosphere and ionosphere model by Grodent and Gérard (2001). This auroral profile is linearly scaled at each time step according to the global pattern of auroral conductance (see SA09). It is this coupled model of the magnetosphere, ionosphere and thermosphere that we use in the present study of the effects of solar wind variability on Jupiter's thermospheric flows. There are some necessary minor differences between the original SA09 model and the version used herein. These will be discussed in Sections 2.6 and 2.7.

The aim of this study is to see how magnetospheric compressions and expansions due to changes in solar wind pressure affect steady-state thermospheric flows and temperatures, and the ensuing effect on predicted Jovian auroral activity. This aspect, as well as the inclusion of a realistic atmospheric model in our study, implies that this is a natural extension of the previous studies that we have mentioned. Our basic approach is as follows. We start with a 'baseline' magnetodisc of equatorial radius, $R_{MM} = 65\ \mathrm{R_J}$, where $R_J = 71492$ km is taken as the radius of Jupiter. We then produce compressed and expanded disc configurations (Section 2.4). Using these magnetospheric models as input to the atmospheric model, we run for 50 Jovian rotations until steady-state is reached.

The theoretical background for our study is given in Section 2. In Section 3 we show and discuss our results, in Section 4 we show cases where our radial current boundary condition is changed, and we summarise the findings in Section 5. At present we run our model until steady-state is reached, but in the future we will aim to simulate the transient, time-dependent effects caused by relatively rapid variations in solar wind pressure and thus magnetospheric size (e.g. Cowley et al., 2007). These rapid variations in solar wind pressure cause significant changes in magnetospheric size, and thus plasma angular velocity, on time scales of 2–3 h. On the other hand, the large inertia of the neutral thermosphere implies that changes in plasma angular velocity would affect the thermosphere on longer time scales, such as $\sim$5–20 h. This condition allows for the approximation that plasma angular momentum is conserved on the shorter time scales associated with solar wind pressure changes (Cowley and Bunce, 2003b). Time-dependent effects are usually neglected in most studies of global energy transport in the Jovian system. Such studies may thus have bearing on the 'energy crisis' at Jupiter that has evaded a definitive answer for four decades, the fact that the planet's exospheric temperatures cannot be maintained by solar heating alone (e.g. Miller et al., 2006). As a first step, the present study focuses on the steady state response of the Jovian thermosphere to different magnetospheric configurations (i.e. different solar wind pressures).

2. Theoretical background

In this section we present a summary of some basic theoretical principles that we use throughout this study. We rely on work that has been conducted in previous studies by Hill (1979), Pontius (1995, 1997), Nichols and Cowley (2004), Cowley et al. (2005, 2007), and SA09.

2.1. Ionospheric currents

The frictional drag due to ion-neutral collisions within the thermosphere causes a lag from corotation of the thermosphere that can be represented by a 'slippage parameter' K (Huang and Hill, 1989):

$$(\Omega_T - \Omega_J) = -K(\Omega_J - \Omega_M) \quad (1)$$

or equivalently

$$(\Omega_T - \Omega_M) = (1-K)(\Omega_J - \Omega_M). \quad (2)$$

Here Ω_M and Ω_J are the angular velocities of the magnetosphere and Jupiter itself (deep planetary angular velocity) respectively. Ω_T is the effective rotation angular velocity of the thermosphere (see SA09). K thus represents the 'slippage' of the neutrals from rigid corotation.

The coupling of the magnetosphere and ionosphere induces an electric field within the thermosphere's rest frame which then causes ionospheric currents to flow. The ionospheric height-integrated Pedersen current density, i_P, and the total, azimuthally

integrated form of this current, $I_P(\theta_i)$, are (Cowley et al., 2007, SA09):

$$i_P = \rho_i \Sigma_P (\Omega_T - \Omega_M) B_i \tag{3}$$

and

$$I_P(\theta_i) = 2\pi \rho_i^2 \Sigma_P (\Omega_T - \Omega_M) B_i, \tag{4}$$

where Σ_P is the height-integrated Pedersen conductance, B_i is the assumed radial ionospheric magnetic field, θ_i is the ionospheric co-latitude, and ρ_i is the perpendicular distance to the planet's magnetic/rotation axis.

Current continuity requires that there also exists in the magnetodisc a radial current density, i_ρ, which can also be azimuthally integrated, represented as I_ρ (Nichols and Cowley, 2004, SA09). We write

$$\rho_e i_\rho = 2\rho_i i_P, \tag{5}$$

$$I_\rho = 8\pi \Sigma_P F_e (\Omega_T - \Omega_M), \tag{6}$$

where $\rho_i = R_i \sin\theta_i$ (R_i is the ionospheric radius), $B_i = 2B_J$ (B_J is the equatorial magnetic field strength at the planet's surface) and the function $F_e(\rho_e) = F_i(\theta_i) = B_J \rho_i^2$ on a magnetic flux shell which intersects the ionosphere at co-latitude θ_i. ρ_e is the equatorial distance from the planet centre to the field lines lying in this shell. We adopt $B_J = 426\,400$ nT as Jupiter's dipole equatorial field (Connerney et al., 1998), and $R_i = 67350$ km as the radius of the polar Pedersen layer (radius of the ionosphere) (Cowley et al., 2007). Note that the auroral ionosphere is at high latitudes, where the planet's radius is $\sim 66\,854$ km at the 1 bar surface. F_e and F_i are the equatorial and ionospheric flux functions respectively (discussed further in Section 2.4). The mapping between θ_i and ρ_e is represented by the equality $F_e(\rho_e) = F_i(\theta_i)$.

Another result of current continuity with regard to the variation of the Pedersen current with latitude is the creation of FACs which flow from the ionosphere to the magnetosphere. The density of these currents (at the ionospheric footpoint of the relevant field line) is

$$j_{\parallel i}(\theta_i) = -\frac{1}{2\pi R_i^2 \sin\theta_i} \frac{dI_P}{d\theta_i}, \tag{7}$$

where $j_{\parallel i}(\theta_i)$ is the FAC density and the sign corresponds to the northern hemisphere where the magnetic field points outward from the planet (Cowley et al., 2007).

2.2. Effective neutral rotation velocity

SA09 define Ω_T as a weighted average of the effective rotation angular velocity throughout the thermosphere–ionosphere. In this section we clarify what is meant by this, for the sake of completeness.

Smith and Aylward (2008) showed that the equatorward current density in the ionosphere consists of two contributions: (1) Pedersen current associated with the azimuthal thermospheric velocity u_ϕ and (2) Hall current associated with the meridional thermospheric velocity u_θ. u_ϕ and u_θ will vary, in general, with altitude z in the thermosphere. We now define a local effective angular velocity ω_T (Smith and Aylward, 2008, SA09) as follows:

$$\rho_i \omega_T = \rho_i \Omega_J + u_\phi + \frac{\sigma_H}{\sigma_P} u_\theta, \tag{8}$$

where σ_P and σ_H are the local Pedersen and Hall conductivities respectively. Integrating over the height of the thermosphere–ionosphere to get the total equatorward current, we find that Ω_T can be defined as

$$\Sigma_P \Omega_T = \int \sigma_P \omega_T \, dz, \tag{9}$$

where Σ_P is the height-integrated Pedersen conductivity

$$\Sigma_P = \int \sigma_P \, dz, \tag{10}$$

where z is altitude. In these expressions Ω_T is a weighted average of the effective neutral angular velocity ω_T throughout the thermosphere-ionosphere, which also contains contributions from meridional winds.

2.3. Energy transfer

In this section we introduce equations which describe the energy transfer from planetary rotation to: (i) magnetospheric rotation and (ii) heating of the neutral atmosphere. According to Hill (2001), the total power per unit area of the ionosphere extracted from planetary rotation, P is given by

$$P = \Omega_J \tau, \tag{11}$$

$$\tau = \rho_i i_P B_i, \tag{12}$$

where τ is the torque per unit area of the ionosphere exerted by the $\boldsymbol{J} \times \boldsymbol{B}$ force. The smaller component of this total used to accelerate the magnetospheric plasma is

$$P_M = \Omega_M \tau. \tag{13}$$

The remainder of this power is dissipated in the upper atmosphere as heat and mechanical work:

$$P_A = (\Omega_J - \Omega_M)\tau. \tag{14}$$

The power P_A consists of two components, as shown by Smith et al. (2005). One of these is Joule heating, P_J, and the other is ion drag power, P_D, which is dependent on the sub-corotation of the neutral atmosphere and is then viscously dissipated as heat. These are given by

$$P_J = (\Omega_T - \Omega_M)\tau \tag{15}$$

and

$$P_D = (\Omega_J - \Omega_T)\tau. \tag{16}$$

These expressions can then be integrated over the appropriate region of the ionosphere to obtain total (global hemispheric) powers.

2.4. Magnetosphere model

The magnetosphere model component used in this study is essentially the same as that used by SA09, based on the Cowley et al. (2005) axisymmetric model for the entire magnetosphere and the more advanced middle magnetosphere model proposed by Nichols and Cowley (2004). The difference between the SA09 model and the one used in this study is that we also use the formalism from Cowley et al. (2007) to calculate equatorial magnetic profiles for compressed and expanded configurations of the magnetosphere. Our coupled model requires as input an equatorial profile of magnetic field strength, along with the corresponding flux function (the flux function is the magnetic flux per radian of azimuth integrated from the given location to infinity). For the axisymmetric, poloidal field models which we employ, surfaces of constant flux function define a shell of field lines with a common equatorial radial distance ρ_e and ionospheric co-latitude θ_i. This allows us to magnetically map the ionosphere to the equatorial plane using $F_i(\theta_i) = F_e(\rho_e)$ (Nichols and Cowley, 2004). The ionospheric form of the flux function is

given by

$$F_i = B_J \rho_i^2 = B_J R_i^2 \sin^2 \theta_i. \quad (17)$$

The equatorial magnetic field in the middle magnetosphere, B_{ze}, and corresponding flux function, F_e, in this region are given by the equations below (Nichols and Cowley, 2004):

$$B_{ze}(\rho_e) = -B_o \left(\frac{R_J}{\rho_e}\right)^3 \exp\left[-\left(\frac{\rho_e}{\rho_{eo}}\right)^{5/2}\right] - A\left(\frac{R_J}{\rho_e}\right)^m, \quad (18)$$

$$F_e(\rho_e) = F_\infty + \frac{B_o R_J^3}{2.5\rho_{eo}} \Gamma\left[-\frac{2}{5}, \left(\frac{\rho_e}{\rho_{eo}}\right)^{5/2}\right] + \frac{AR_J^2}{m-2}\left(\frac{R_J}{\rho_e}\right)^{m-2}, \quad (19)$$

where $B_o = 3.335 \times 10^5$ nT, $\rho_{eo} = 14.501$ R_J, $A = 5.4 \times 10^4$ nT, $m = 2.71$, $F_\infty \approx 2.841 \times 10^4$ nT R_J^2, and $\Gamma(a,z) = \int_z^\infty t^{a-1}e^{-t}\,dt$ is the incomplete gamma function. These parameters represent an analytical fit to spacecraft magnetometer data (Connerney et al., 1981; Khurana and Kivelson, 1993). The magnetic field model has a grid resolution of 0.01 R_J which, when magnetically mapped to the ionosphere, produces footprints of the field lines separated by angles equal to or smaller than the thermospheric model's latitudinal grid spacing. This is a sufficient condition to sample realistic FAC profiles and thermospheric flow patterns within the ionospheric part of the model.

Using Eqs. (18) and (19) as a starting point we are able to calculate model magnetic fields and flux functions corresponding to states of differing magnetospheric size. These models are valid within the range of $\sim 5R_J$ to near the magnetopause, however, in this study we employ a middle magnetosphere with maximum radial distance of 85 R_J. Cowley et al. (2007) assume that Jupiter's magnetosphere consists of two components; the middle and the outer regions. They take the equatorial magnetic field strength in the outer magnetosphere (beyond 65 R_J for their 'baseline' case) to be constant between ~ 5 and ~ 15 nT. Using Eqs. (18) and (19), valid only within the middle magnetosphere, we apply their method of compressing and expanding this region's magnetic field configuration. We then use our middle magnetosphere field model to obtain solutions for plasma angular velocity Ω_M in this region (Section 3.1.1). For the outer magnetosphere we shall use constant, assumed values of Ω_M.

Using the principles of magnetic flux conservation described by Cowley et al. (2007), we were able to calculate equatorial field profiles for Jupiter's magnetosphere for different values of solar wind dynamic pressure. To compress (resp. expand) a magnetodisc (middle magnetosphere) from an initial radius R_{MMO}, a uniform southward (resp. northward) perturbation field, ΔB_z, is applied to our initial magnetospheric model (described by Eqs. (18)–(19)). The formalism in Cowley et al. (2007) enables us to calculate ΔB_z as a function of magnetodisc radius R_{MM}. At a given R_{MM} ('final' disc radius), the flux conservation condition is

$$-\pi R_{MM}^2 \Delta B_z = 2\pi(F_O(R_{MM}) - F_O(R_{MMO})), \quad (20)$$

where F_O is the initial profile of the flux function (given by Eq. (19)). Rearranging to solve for ΔB_z:

$$\Delta B_z = \frac{-2\Delta F}{R_{MM}^2}, \quad (21)$$

where $\Delta B_z < 0$ for a southward field perturbation, and

$$\Delta F = F_O(R_{MM}) - F_O(R_{MMO}). \quad (22)$$

Using Eqs. (18)–(22) we calculated equatorial magnetic field and flux function profiles for three different magnetospheric configurations, namely a compressed system, case A with $R_{MM} = 45$ R_J, a baseline system, case B with $R_{MM} = 65$ R_J and case C, an expanded system with $R_{MM} = 85$ R_J. We choose $R_{MM0} = 65$ R_J (as used by Cowley et al., 2007). These configurations are listed in Table 1 and the respective profiles are shown in Fig. 1.

Fig. 1a shows how the magnetic field strength varies with equatorial distance in the magnetodisc for the three cases. The dotted and dashed lines show compressed (case A) and expanded (case C) magnetic field profiles respectively. Case A with a disc

Table 1
Table showing the three different magnetospheric configurations used in this study. The radii of the magnetodisc R_{MM} and magnetopause R_{MP} are shown along with the values of the perturbation field. Note R_{MP} is calculated as in Cowley et al. (2007). Solar wind dynamic pressure (P_{SW}) is also shown for both Joy et al. (2002) and Huddleston et al. (1998) magnetopause models (J or H respectively).

Case	A	B	C
R_{MM}/R_J	45	65	85
R_{MP}/R_J	75	86	101
ΔB_z/nT	−1.16	0.0	0.19
$P_{SW\,J}$/nPa	0.121	0.060	0.020
$P_{SW\,H}$/nPa	0.034	0.018	0.008

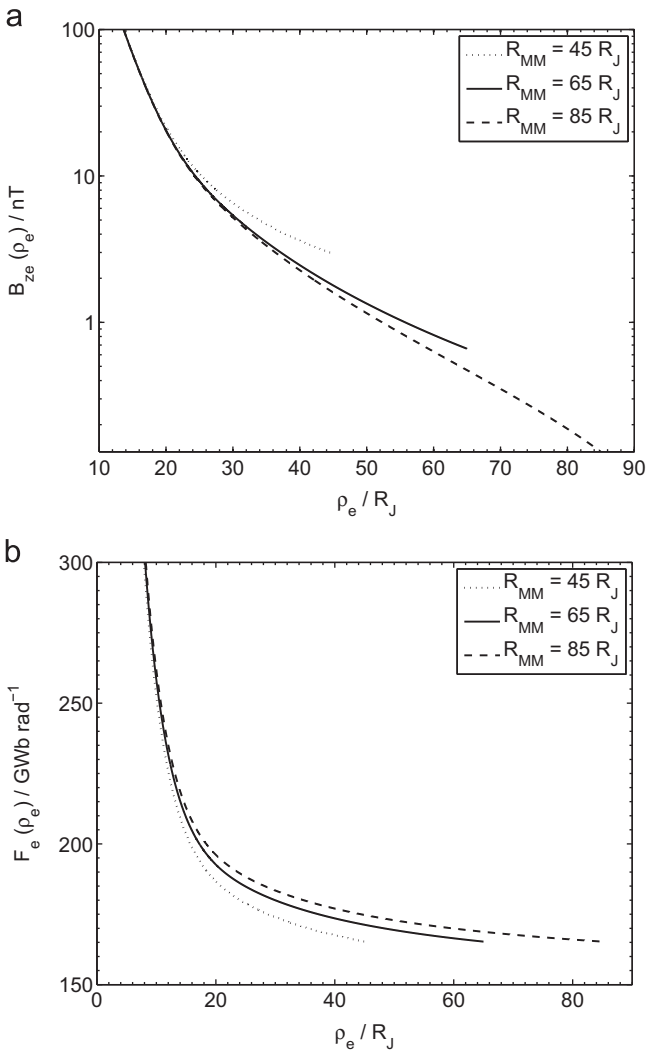

Fig. 1. (a) Variation of the magnetic field strength (log scale) with equatorial radial distance within the magnetodisc for the three configurations used. Case A is represented by the dotted line, whilst cases B and C are represented by the solid and dashed lines respectively. (b) The corresponding flux functions for the three magnetospheric cases are plotted against equatorial radial distance using the same line code.

radius of $R_{MM}=45\ R_J$ corresponds to a relatively high solar wind pressure and a strong equatorial magnetic field. Case C, representing a relatively low solar wind pressure has a magnetodisc radius of $R_{MM}=85\ R_J$ and a comparatively weak magnetic field. Fig. 1b shows how the corresponding flux functions vary with equatorial distance. By definition the value of the flux function at $\rho_e=R_{MM}$ has the same value for all cases.

2.5. Ionosphere model

For simplicity, we use an auroral ionosphere model from the literature to derive a global conductivity model. This conductivity model consists of both vertical and horizontal variations which we shall briefly summarise in Sections 2.5.1 and 2.5.2. For a more detailed description of the conductivity model employed, the reader is referred to the following studies, SA09, Nichols and Cowley (2004) and Grodent and Gérard (2001).

2.5.1. Vertical dependence of conductivity

The one-dimensional auroral ionosphere model by Grodent and Gérard (2001) (hereafter GG) developed for Jupiter, is used to establish the altitude dependence of ionospheric conductivity. The auroral model uses a two-stream electron transport code to calculate auroral electron and ion densities. There are two versions of this model, i.e. 'diffuse' and 'discrete' but for our studies, both versions produce similar results. Consequently, the diffuse version is used, as it covers a greater region of the main auroral oval and polar cap.

The GG model outputs Pedersen and Hall conductivity profiles for a specific thermal structure. However, our thermosphere model has a variable thermal structure which is a function of latitude. In order to maintain realistic height-integrated conductivities in the model, at each pressure level we calculate the conductivity per unit mass as follows (SA09):

$$s_i=\frac{\sigma_i}{\rho}, \tag{23}$$

where $i=P$ or H representing Pedersen or Hall, σ is the conductivity and ρ is the neutral mass density. Adjacent pressure levels enclose constant masses of thermospheric gas (hydrostatic equilibrium assumption). Therefore, the height-integrated Pedersen (Σ_P) and Hall (Σ_H) conductivities depend solely on the profiles of s_i with respect to pressure and not thermal structure. This leads to a Pedersen conducting layer, which we define as the region with conductivity greater than 10% of the Pedersen conductivity at the auroral ionisation peak, located at pressures of $\sim$0.8–0.04 μbar or at altitudes of $\sim$350–600 km above the 1 bar level.

2.5.2. Horizontal conductivity model

The height-integrated conductivity in the inner and middle magnetospheres is dependent on the FAC density according to the following equations (Nichols and Cowley, 2004):

$$\Sigma_P(j_{\parallel i})=\Sigma_{PO}+\Sigma_{Pj}(j_{\parallel i}), \tag{24}$$

where

$$\Sigma_{Pj}(j_{\parallel i})=0.16j_{\parallel i}+\left\{2.45\left[\frac{(j_{\parallel i}/0.075)^2}{1+(j_{\parallel i}/0.075)^2}\right]\times\frac{1}{[1+\exp(-(j_{\parallel i}-0.22)/0.12)]}\right\}, \tag{25}$$

where $\Sigma_{PO}=0.0275$ mho (Nichols and Cowley, 2004) is the background conductivity due to solar photoionisation, and $\Sigma_{Pj}(j_{\parallel i})$ in mho is an auroral enhancement due to the FAC density $j_{\parallel i}$ in μA m^{-2}. The dependence of Σ_H on $j_{\parallel i}$ is calculated from Eq. (25) using standard formulae (e.g. Kivelson and Russell, 1995, p. 201). The total conductivity in the ionisation region is dominated by Σ_P due to the small values of Σ_H.

In the outer magnetosphere and polar cap regions, conductivity enhancement is likely to be present since UV and IR auroral emissions are detected in these regions. Cowley et al. (2005) set $\Sigma_P=0.2$ mho (effective Pedersen conductivity) in these regions in accordance with the theory of Isbell et al. (1984). To allow for comparison, we employ the same conductivity value in these regions.

2.6. Coupled model

We couple our magnetosphere model with a global numerical model of the thermosphere and a global conductivity model of the ionosphere as described in SA09 and Section 2.5. The resolution of the model grid is 0.2° in latitude, and 0.4 pressure scale heights in the vertical direction. That is, we use pressure as a vertical coordinate, with the lower boundary at 2 μbar (300 km above the 1 bar level) and the upper boundary at 0.02 nbar. Altitudes are updated in the model assuming hydrostatic equilibrium. For simplicity all models are axisymmetric with respect to the planet's axis of rotation. This assumption does not greatly influence the basic physics underlying the conclusions of this study (SA09). It is important to emphasise that the assumption of axisymmetry implies zero azimuthal gradients in the model variables. This allows us to represent model outputs in two-dimensions (latitude and altitude) while still using the three-dimensional Navier–Stokes equations.

Section 6 in SA09 describes the method of coupling the magnetosphere, thermosphere and ionosphere models. We employ essentially the same method, with a few minor changes. The same value of the Jovian radius, $R_J=71492$ km is used for both our flux function calculations and atmospheric modelling. The coupled model in SA09 ran for 200 Jovian rotations to reach steady-state. Comparisons of height, temperature and azimuthal velocity in the inertial frame data for case B were made for run-times of 200 and 50 rotations. Calculations show that between both run-times there was a maximum relative difference of $\sim$0.4%, $\sim$0.8% and $\sim$1.2% for height, temperature and azimuthal velocity respectively. This difference causes no significant change in any other parameters obtained from the model and running the model for 50 rotations would save considerable CPU time. Thus for the purposes of this study, running the model for 50 rotations was considered sufficient to reach steady state.

2.7. Solving the coupled equations of thermospheric and magnetospheric momentum

Studies such as Hill (1979) and Pontius (1997) have shown that for the middle magnetosphere to be in a steady state, the radial gradient of the outward angular momentum flux of iogenic plasma must be equal in magnitude to the torque per unit radial distance on that plasma. The plasma model that describes the middle magnetosphere is based on four equations:

$$\frac{1}{\rho_e}\frac{d}{d\rho_e}(\rho_e^2\Omega_M)=\frac{8\pi\Sigma_P F_e|B_{ze}|}{\dot{M}}(\Omega_T-\Omega_M), \tag{26}$$

$$j_{\parallel i}=\frac{4B_J}{\rho_e|B_{ze}|}\frac{d}{d\rho_e}[\Sigma_P F_e(\Omega_T-\Omega_M)], \tag{27}$$

$$\Sigma_P=\Sigma_P(j_{\parallel i}), \tag{28}$$

$$\Omega_T=\Omega_T(\Omega_M,\Sigma_P), \tag{29}$$

where $\dot{M}=1000\ \mathrm{kg\ s^{-1}}$ is the assumed mass outflow rate from the Io torus and $j_{\parallel i}$ is the upward FAC density in the ionosphere.

These equations describe the inter-dependence of magnetospheric angular momentum per unit mass ($\rho_e^2\Omega_M$), FAC density

($j_{\parallel i}$) and Pedersen conductance (Σ_P). Eq. (29) represents the output from the thermospheric model component, which is forced by magnetospheric inputs of $\Omega_M(\rho_e)$. Eq. (26) is the Hill–Pontius equation (Hill, 1979; Pontius, 1997) with a modification by SA09 to include effects of neutral thermosphere flow, represented by Ω_T. This equation balances torques caused by the outward diffusion of the disc plasma and the $\boldsymbol{J} \times \boldsymbol{B}$ force associated with the magnetosphere-ionosphere coupling currents. Eq. (27) is used to calculate the FAC in the ionosphere. An increase in field-aligned current should have an effect on angular velocities $\Omega_M(\rho_e)$, through enhancement of the ionospheric conductivities. We account for this in Eq. (28), representing Eqs. (24) and (25), which describes how enhancements in $j_{\parallel i}$ also affect the Pedersen conductance Σ_P (higher flux of precipitating auroral electrons increases the production rate of ionospheric plasma).

Our method for solving these equations is the same as that in SA09 and Nichols and Cowley (2004) (who originated this model). This is essentially a shooting method which varies the value of Ω_M at the outer edge of the disc until the solution, integrated inwards from this location, smoothly joins an appropriate 'inner disc' analytical solution at 12 R_J. We set the azimuthally integrated radial current at the outer edge of the disc to a value of 100 MA as our outer boundary condition (following Nichols and Cowley, 2004), whilst we have near-rigid corotation of plasma as an inner boundary condition. We need, however, to ensure that the height-integrated Pedersen conductivities at the poleward ionospheric boundary of the magnetodisc field line region, Σ_P(disc), and at the equatorward boundary of the outer magnetosphere region, Σ_P(outer), join smoothly together to avoid discontinuities at this interface. This is particularly important for large compressions such as that of case A. A Gaussian function was used to extrapolate Σ_P from the magnetodisc into the outer magnetosphere region. We ensured the Gaussian function would terminate with a polar value equal to the chosen background Σ_P in the outer magnetosphere, and that this transition would occur with a small latitudinal scale (0.2°). The amplitude and centre of the Gaussian function were calculated using the gradient of $d\Sigma_P/d\theta$ at the poleward edge of the disc region. We further discuss the resulting profiles of Σ_P in Section 3.1.2.

3. Results and discussion

In this section we present the results obtained from our modelling. We first discuss results concerning angular velocities, conductivities and currents. Then we proceed to discuss the thermospheric flows and energies.

3.1. Angular velocities, conductivities and currents

3.1.1. Angular velocities

Combining models from Nichols and Cowley (2004) and Cowley et al. (2005) of the middle and outer magnetospheres, one can essentially divide the entire magnetosphere into four regions, labelled I–IV. The Dungey-type interaction of the polar open field lines with the solar wind takes place in region I. The closed field lines of the outer magnetosphere are involved in Dungey and Vasyliunas cycles (associated with mass loss from the disc) in region II. Regions III (shaded region in figures) and IV represent the middle magnetosphere (magnetodisc) and the corotating inner magnetosphere respectively (see Fig. 2). As stated in Section 2.2, Ω_T is a weighted average of the effective angular velocity throughout the thermosphere–ionosphere, computed over all altitudes at each co-latitude θ_i. Ω_M in region I has a constant value of $\sim 0.1\Omega_J$ (Isbell et al., 1984). Region II also has a fixed value of Ω_M that depends on magnetospheric size, in accordance with observations (Cowley et al., 2007). The profiles of Ω_M in regions I, II and III are joined smoothly across their boundaries with the use of hyperbolic tangent functions. The plasma angular velocity profiles for regions III and IV are calculated using Eqs. (26)–(29) by the model.

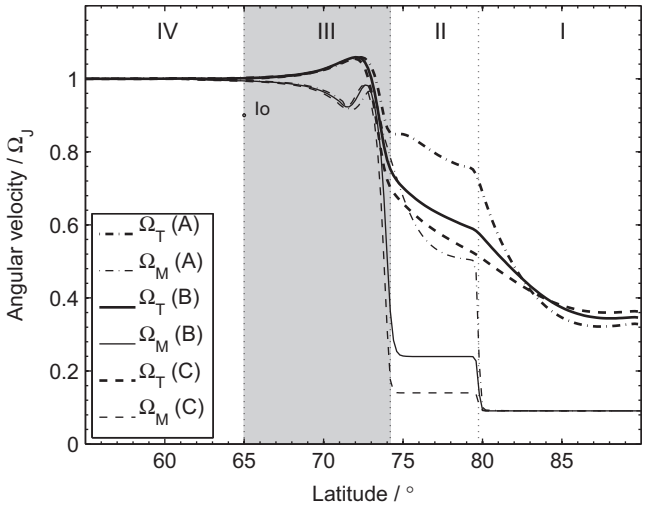

Fig. 2. Thermospheric and magnetospheric angular velocities for cases A–C are plotted in the high latitude region and are represented by thick and thin lines respectively. Dot-dashed lines represent case A, solid case B and dashed case C. The black dot labelled 'Io' indicates the magnetically mapped position of the moon Io's orbit in the ionosphere. The magnetospheric regions (region III is shaded) considered in this study are labelled and separated by the dotted black lines.

Fig. 2 shows how the thermospheric (thick lines) and magnetospheric (thin lines) angular velocities vary in Jupiter's high latitude region for our three cases. We also show the region boundaries used in our model and the magnetically mapped location of Io in the ionosphere. Case B, our 'baseline' is represented by the solid lines. At low latitudes, rigid corotation with Jupiter's deep atmosphere is maintained. At the higher latitudes ($>60°$) the magnetosphere (represented by Ω_M) sub-corotates to a greater degree than the thermosphere (expressed by Ω_T). The shape of these Ω_M and Ω_T profiles are similar to those obtained in the studies of SA09. Ω_M and Ω_T profiles for case C, our expanded case, are represented by dashed lines. These profiles resemble those of case B but they possess slightly smaller angular velocities in region II. For case A, Ω_M and Ω_T are shown by the dot-dashed lines. Both Ω_M and Ω_T indicate sub-corotation to a lesser extent than the respective profiles from cases B and C, in agreement with the study of Cowley et al. (2007) who modelled Ω_M, assuming simplified profiles for Ω_T (where $K=0.5$). We thus show that the thermosphere and magnetosphere for compressed configurations corotate to a greater degree than in the case of expanded configurations. Our plotted profiles quantify this result for both Ω_M and Ω_T.

3.1.2. Conductivities and currents

Previous studies of the effect of solar wind-induced compressions and expansions of Jupiter's magnetosphere have shown that magnetospheric compressions reduce ionospheric and parallel currents (in the steady state). Expansions on the other hand, have the opposite effect due to the increased transport of angular momentum to the magnetosphere (Southwood and Kivelson, 2001; Cowley and Bunce, 2003a; Cowley et al., 2007). Our profiles in Fig. 2 confirm and quantify the expected angular velocity profiles of both the thermosphere and magnetospheric plasma in the steady state, when the rate of addition of angular momentum to the plasma (at a given radial distance), due to the

magnetosphere–ionosphere currents, exactly balances the rate of removal due to the radial plasma outflow. We consider the solutions for Ω_M and Ω_T in more detail in Section 3.1.1. The weaker average magnetic field for the expanded cases, combined with the finite ionospheric conductivity, leads to lower Ω_M values, despite increased rates of angular momentum transport in the system. In this section we present our quantitative findings regarding ionospheric conductivities and currents for the different magnetospheric configurations of our coupled system.

The variation of height-integrated true Pedersen conductivity Σ_P for our three magnetospheric cases is shown in Fig. 3a, where cases A–C are represented by the dot-dashed, solid and dashed lines respectively. The magnetically mapped location of Io in the ionosphere is shown by the black dot and the magnetospheric regions used in this study are marked and separated by black dotted lines. All three cases have peaks just equatorward of the region III/II boundary—characteristic features of the Ω_M solutions (Eqs. (26)–(29))—and then fall to the assumed conductivity value in regions II and I. Cases B and C have similar profiles and peak values close to those calculated in SA09, whilst case A has a peak that is significantly higher than both of these cases. The profile for case A resembles that from Nichols and Cowley (2004) for the near-rigid corotation approximation where $(1-\Omega_M/\Omega_J) \ll 1$, which are conditions met by case A in regions IV and III. Another feature that distinguishes case A is that the peak conductivity is shifted poleward slightly compared to cases B and C. This is partly due to the model method which connects the Pedersen conductivity in region III with the fixed value in region II for case A (see Section 2.7). The poleward shift is also due to the higher Σ_P required in case A in order to achieve the prescribed value of radial current at the outer edge of the magnetodisc (poleward boundary of region III) (see Section 2.7).

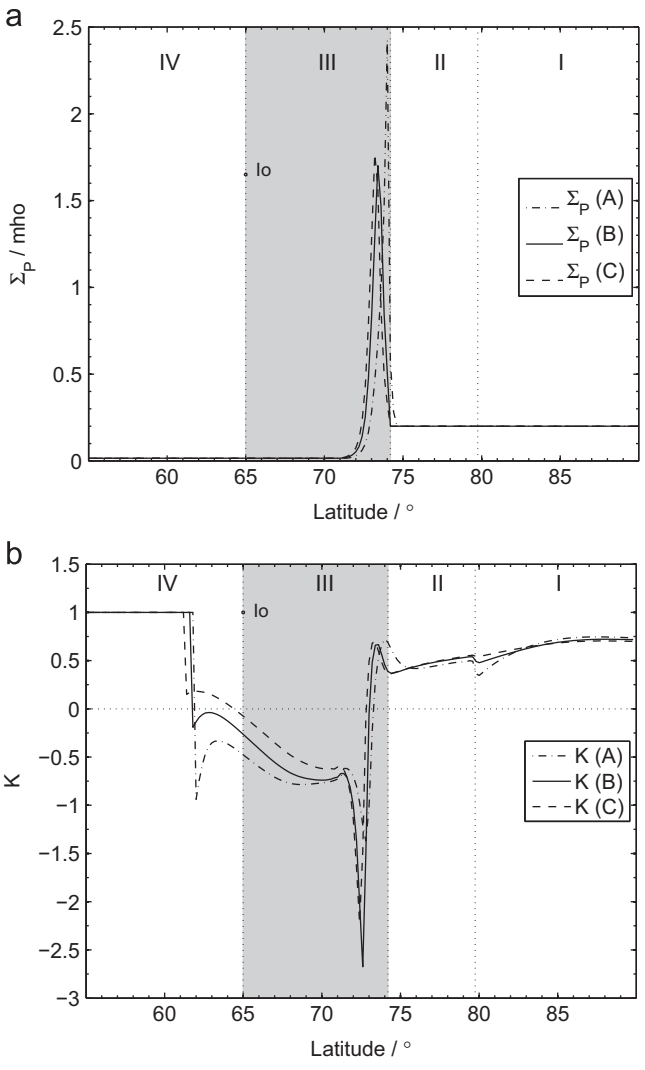

Fig. 3. (a) Height-integrated Pedersen conductivities for cases A–C plotted versus latitude. Cases A–C are represented by dot-dashed, solid and dashed lines respectively. The magnetically mapped location of Io in the ionosphere is labelled and marked by the black dot. Magnetospheric regions (region III is shaded) are labelled and separated by dotted black lines. (b) 'Slippage' parameter K plotted versus latitude for cases A–C. The line code for cases A–C remains the same as (a).

Fig. 3b shows how the slippage parameter K varies with latitude for our three magnetospheric cases. The profiles for K indicate the ratio between thermospheric and magnetospheric angular velocities with respect to Jupiter's planetary rotation velocity ($K=(\Omega_J-\Omega_T)/(\Omega_J-\Omega_M)$). Positive values for K represent situations when both the thermosphere and magnetosphere are sub-corotating or super-corotating with respect to the planet, as seen in regions IV, II and I. Negative K values represent situations where the thermosphere and magnetosphere are undergoing opposing motions, i.e. one is super-corotating whilst the other is sub-corotating. This is seen just equatorward of Io's magnetic footprint on the ionosphere and for the latitudinal majority of region III. This distinction is important because the last half degree of latitude in region III maps to the largest part of the equatorial magnetosphere.

Fig. 4a shows the corresponding variation of azimuthally integrated Pedersen current with latitude. The line code is the same as that in Fig. 2. Profiles for cases B and C follow a similar trend to the steady-state Pedersen current profiles in Cowley et al. (2007), whilst the profile for case A is different within regions III and II, due to conditions comparatively nearer to corotation.

Fig. 4b shows the azimuthally integrated radial currents through the magnetospheric equator for all three cases in regions IV and III and how they vary with radial distance. The radial currents for cases B and C show a 's-curve' structure which is consistent with previous studies such as SA09. Case A, however, shows a more linear relation between the equatorial radial distance and azimuthally integrated radial current which is not seen in the more expanded case of SA09 but is consistent with the near-rigid corotation approximation conditions presented in Nichols and Cowley (2004). As previously noted, this near-rigid corotation condition applies to case A throughout regions IV and III. We also note that, as mentioned in Section 2.7, our outer boundary condition is that the radial current value at the region III/II boundary is 100 MA. The case A curve in Fig. 4b does not quite reach this value due to the joining of the Pedersen conductivity across regions III and II (see Section 2.7). A hyperbolic tangent function is used to smoothly join the Perdesen conductivity across regions II and III, using information from a few points either side of this boundary. This leads to a smoothing of the disc solution near its outer edge, leading to a slightly different value of the azimuthally integrated radial current at this location. This curve does demonstrate, however, that I_P and I_ρ in case A have to increase very rapidly in the outer magnetodisc in order to satisfy the boundary condition. Since there is no a priori reason why $I_{\rho\infty}$ should be independent of magnetosphere size, we will also investigate, later, the effect of varying the boundary condition upon the resulting profiles of current and angular velocity (Section 4).

FAC densities are plotted against latitude in Fig. 5. For all three cases, FAC densities have three positive peaks, the first two lying on either side of the region III/II boundary and the third lying on the region II/I boundary. Positive peaks correspond to upward directed FACs that produce aurorae. At the boundary between

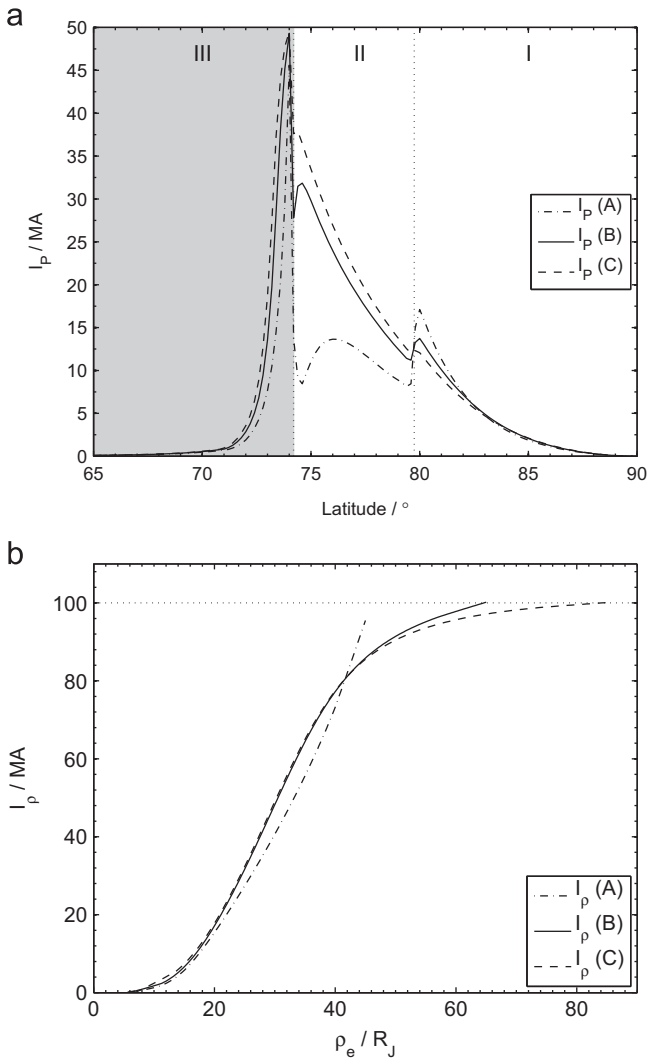

Fig. 4. (a) Azimuthally integrated Pedersen current shown as a function of latitude for cases A–C. Case A is represented by the dot-dashed line, case B by the solid line and case C by the dashed line. The magnetospheric regions (region III is shaded) are also marked and separated by the dotted black lines. (b) Azimuthally integrated radial current plotted against equatorial radial distance from Jupiter for cases A–C. The line code is the same as in (a).

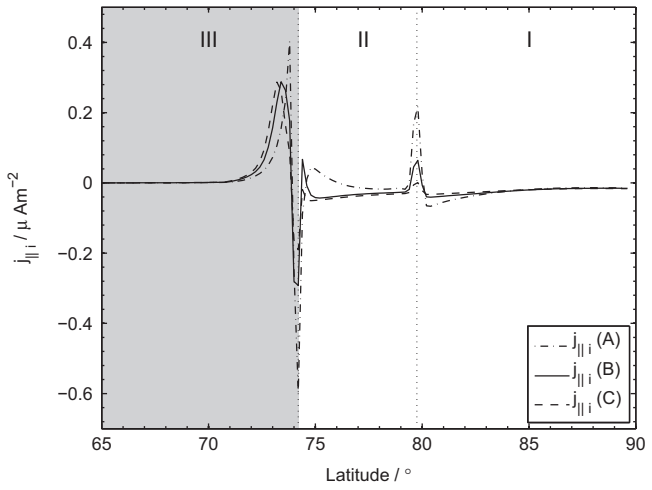

Fig. 5. FAC densities in the high latitude region for cases A–C. Dot-dashed lines represent FACs for case A whilst solid and dashed lines represent FACs for cases B and C respectively. The magnetospheric regions (region III is shaded) are labelled and separated by black dotted lines.

region III and II, the negative peaks indicate strong downward-directed FACs whose magnitude is dependent on the equatorial radius of region III (R_{MM}). The main auroral oval is represented by the peak at $\sim 73^\circ$ latitude. Our model suggests that there would also be weaker more distributed aurorae poleward of the main oval, represented by the second and third peaks at $\sim 75^\circ$ and $\sim 80^\circ$ respectively. A relatively dark region would arise from the trough at $\sim 74^\circ$ latitude, creating 'dark rings'. The latter feature is also obtained in previous studies by Cowley et al. (2005, 2007) but at present, we lack the observations required to constrain the value of $j_{\parallel i}$ downward. The strong downward FACs at $\sim 74^\circ$ are due to the significant changes in Pedersen current on crossing the boundary between regions II and III, which in turn is due to the changes in magnetospheric and thermospheric angular velocities. The Pedersen conductivity in the model also changes significantly across this boundary, which also contributes to a large magnitude for $j_{\parallel i}$. The strongest downward FACs in our calculations are even less constrained by observations, but they also occur in the modelling of Tao et al. (2009) who also used a coupled magnetosphere-thermosphere approach.

Our calculations shown in Figs. 2–4 all support the expected trends described by Southwood and Kivelson (2001). The angular velocity profiles (Fig. 2) for both the thermosphere and magnetodisc show that there is a greater degree of sub-corotation for more expanded magnetospheres, corresponding to lower solar wind dynamic pressures. This is due to the thermosphere being able to transfer momentum to a compressed magnetosphere (stronger field) with greater efficiency than a larger, expanded one. The Pedersen conductivities (Fig. 3a), FAC densities (Fig. 5) and azimuthally integrated Pedersen and radial currents (Fig. 4a and b) all show an increase in region III (shaded) for expanded magnetospheres. In this region, the integrated auroral FAC for case A is $\sim$50–60% of that cases B and C suggesting that auroral emission would be greater for an expanded magnetosphere than a compressed one. Our currents naturally have similar values to those obtained in SA09. They also show similar trends and profiles to studies such as those of Cowley et al. (2005, 2007) and Tao et al. (2009). Our study is an extension of these works in the sense that we use an atmospheric circulation model coupled to three distinct magnetospheric configurations.

3.2. Thermospheric flows and energies

Fig. 6 shows momentum balances for our compressed and expanded configurations in both the low and high altitude regions. Fig. 7 shows the thermospheric flows, temperature distributions and power dissipated per unit area for all three model configurations. Results for each case are displayed in the columns of the figure.

3.2.1. Thermospheric flows

According to SA09, meridional advection is the main process by which angular momentum is transferred to the high latitude thermosphere. Advection (combination of the horizontal and vertical advection of momentum by winds blowing along and across fixed pressure surfaces) is just one of the means by which momentum is changed at a fixed location within the thermosphere. In Fig. 6 we present force balance diagrams at low (a and b) and high (c and d) altitudes for cases A and C. The force colour codes are in the figure caption. Considering the high altitude region first, advection and other zonal force components (ion drag and Coriolis) are small. Thus,

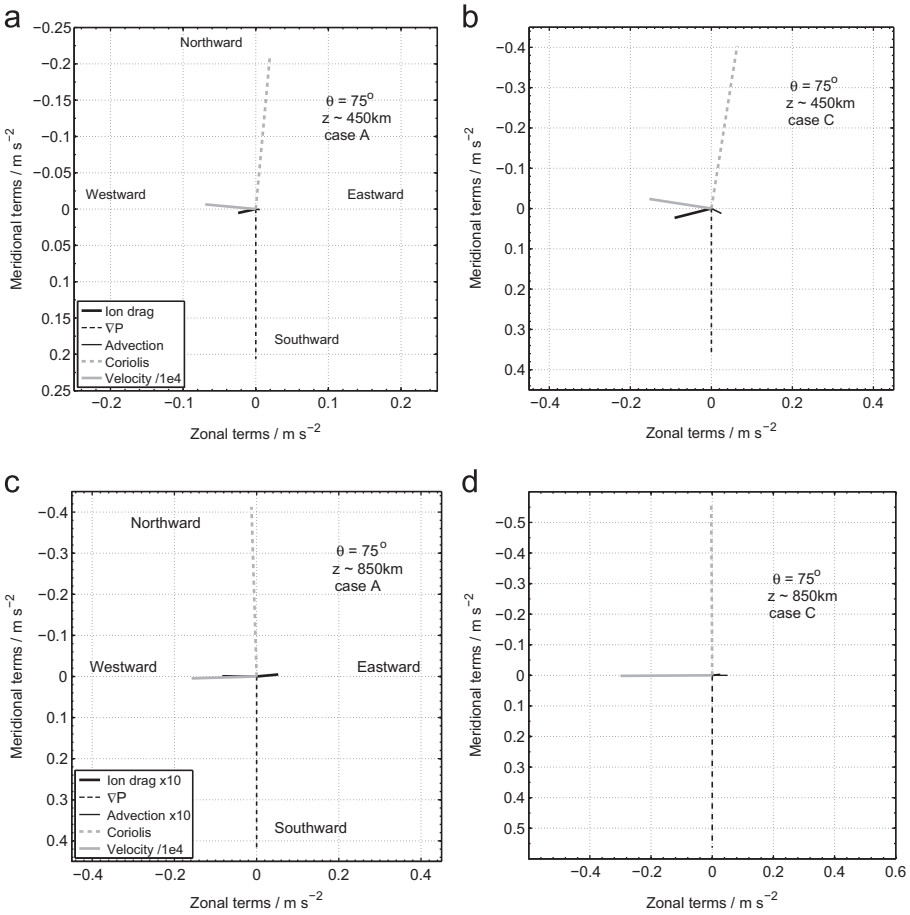

Fig. 6. Force balance diagrams for cases A (left column) and C (right column) at ionospheric co-latitude of 75°. (a) and (b) show meridional and zonal force balance in the low altitude region whilst (c) and (d) show meridional and zonal force balance in the high altitude region. Ion drag forces are represented by thick black solid lines, fictitious (Coriolis) forces by thick light grey dashed lines, pressure gradient by thin black dashed and advection by the thin black solid lines. The velocity vector is also plotted and is represented by the thick light grey lines. Note that the magnitude of velocity components have been divided by a factor of 1×10^4 to fit the plotted scale and that in (c) and (d) the components of ion drag and advection have been multiplied by a factor of 10 to increase visibility.

the pressure gradient is balanced almost perfectly by the Coriolis force. This force balance creates a sub-corotational flow with a small equatorward component. We now consider low altitudes near the Pedersen conductivity peak, where the ion drag term $\boldsymbol{J} \times \boldsymbol{B}$ is strong. Coriolis, pressure gradient and ion drag forces are not balanced. Thus, a significant advection term arises to restore equilibrium, resulting in a region of strong poleward acceleration (see Fig. 7d–f). The resulting meridional flow at low altitudes is thus polewards and transports heat to the polar region.

Fig. 7a–c shows how the thermospheric azimuthal velocity in the corotating reference frame varies within the high latitude region for the different cases. Positive (resp. negative) values of neutral azimuthal velocity indicate super (resp. sub)-corotating regions. Arrows indicate the direction of meridional flow, and the white line the locus of rigid corotation. The magnetospheric region boundaries are plotted with the dotted black lines. We can see a broad azimuthal jet (blue area) in regions I and II that sub-corotates to a greater degree with an increase in magnetospheric size. Also present is a super-corotational jet (dark red region) just equatorward of the region III/II boundary, visible in Fig. 2. Ion drag (see Fig. 6) gives rise to the sub-corotational azimuthal flows seen in regions I, II and III. As the magnetosphere expands, the $\boldsymbol{J} \times \boldsymbol{B}$ term increases and azimuthal flows sub-corotate to an even greater degree. Advection forces arise due to the lack of equilibrium at low altitudes, causing an accelerated poleward flow whose velocity increases by $\sim 90\%$ from case A to C. The effect of advection can be seen in Fig. 7d–f, which shows meridional flows in the high latitude region. This accelerated flow transports energy from Joule heating, depositing it at higher latitudes and forming a polar 'hot spot' (Smith et al., 2007). Super-corotation occurs at latitudes where zonal ion drag and advection forces are negligible compared to the Coriolis force, which can then accelerate the flow beyond corotation. At high altitudes, forces are essentially balanced. Thus high altitude zonal flows now have an equatorward component. Therefore, meridional flows show a poleward low-altitude flow and an equatorward high-altitude flow consistent with the previous studies of Smith et al. (2007) and SA09.

Fig. 7g–i shows thermospheric temperature distributions. The temperature scale is shown on the colour bar. Magenta and solid grey contours enclose areas where Joule heating and ion drag energy inputs exceed 20 W kg^{-1} and dashed grey contours highlight regions where ion drag decreases kinetic energy at a rate greater than 20 W kg^{-1}. A uniform rate of 20 W kg^{-1} gives an integrated energy input rate of the order of 100 mW m^{-2} (1 ergs cm^{-2} s^{-1} = 1 mW m^{-2}) within the Pedersen conducting layer. This integrated rate is of a similar order of magnitude to the estimated total IR auroral emission (200 ergs cm^{-2} s^{-1} from Drossart et al., 1993). We see significant energy input from Joule heating and ion drag at low altitudes and between 73° and 85°

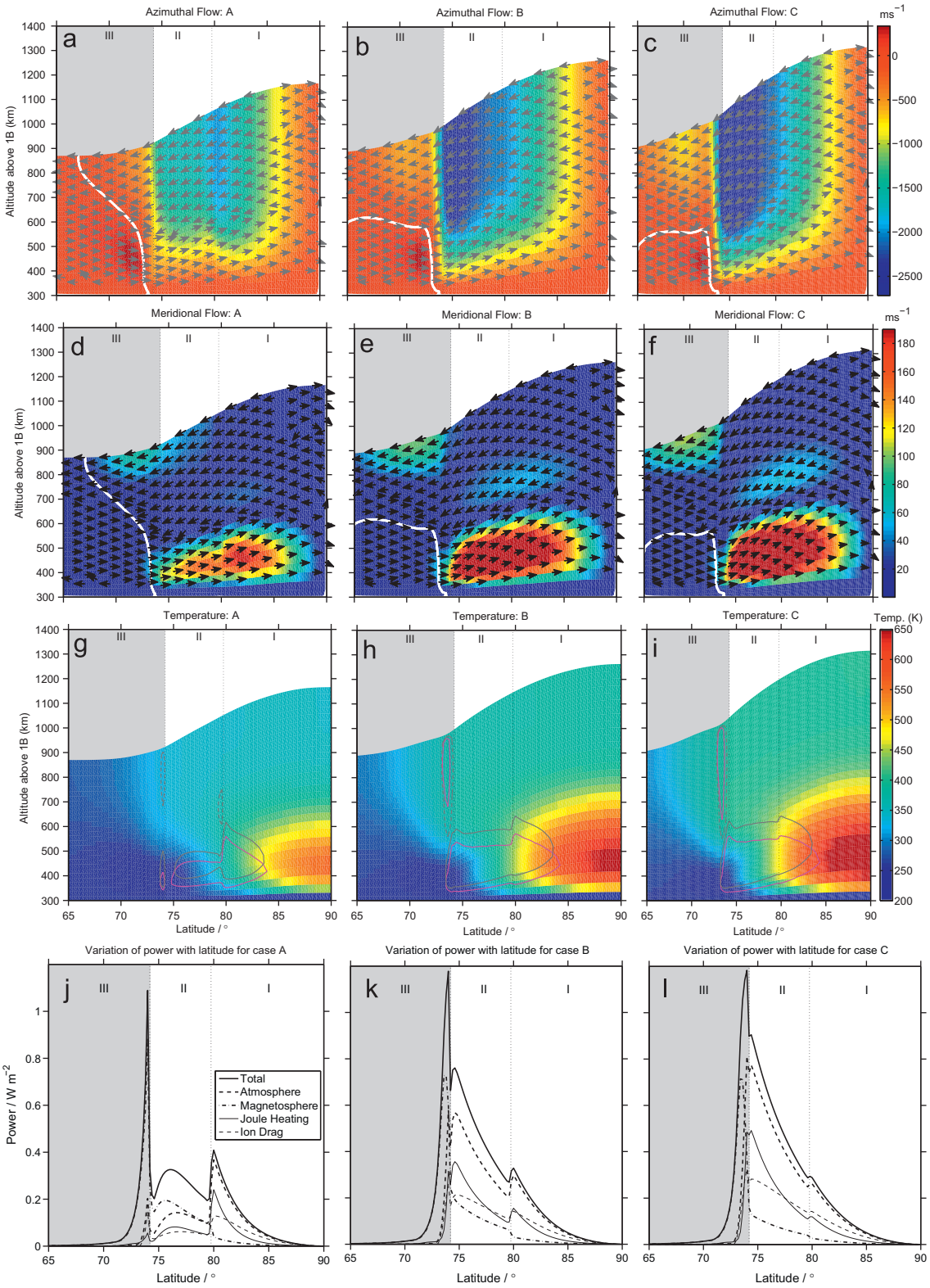

Fig. 7. (a)–(c) show the variation of thermospheric azimuthal velocity (colour scale) in the corotating reference frame for cases A–C respectively. Positive values dark red represent super-corotation, whilst negative values (light red to blue) represent sub-corotation. The direction of meridional flow is indicated by the arrows and the white line represents the locus of rigid corotation. Magnetospheric regions (region III is shaded) are labelled and separated by black dotted lines. (d)–(f) show the meridional velocity in the thermosphere for cases A–C. The colour scale indicates the speed of flows. Other labels and lines are as for (a)–(c). (g)–(i) show thermospheric temperature distributions. Magenta contours enclose regions where Joule heating exceeds 20 W kg^{-1}, solid grey contours enclose regions where ion drag increases the kinetic energy at rates exceeding 20 W kg^{-1} and dashed grey contours enclose regions where ion drag decreases the kinetic energy at rates greater than 20 W kg^{-1}. (j)–(l) show how the power per unit area varies for cases A–C. The thick solid line represents total power which is the sum of magnetospheric power (thick dot-dashed line) and atmospheric power (thick dashed line); atmospheric power is the sum of both Joule heating (thin solid line) and ion drag (thin dashed line). Other labels are as for (a)–(c).

latitude due to their dependence on the strength of the current density $\boldsymbol{j}$. $\boldsymbol{j}$ is proportional to the difference between local thermospheric and plasma angular velocity, and to the Pedersen conductivity σ_P which peaks at low altitudes. There lies a narrow region of high altitude Joule heating just equatorward of the region III/II boundary in expanded cases due to the large shear between Ω_T and Ω_M. The decrease in kinetic energy (grey dashed lines) occurs as the ion drag force now acts to accelerate thermospheric flows towards corotation (see Fig. 6c and d where ion drag is eastwards). The remaining feature of prominence is the large 'hot spot' at low altitudes in region I as discussed above. The peak temperature of the 'hot spots' increase from $\sim$560 K in case A to $\sim$695 K in C.

3.2.2. Atmospheric and magnetospheric energy 'budget'

Fig. 7j–l presents the total, magnetospheric, atmospheric, ion drag and Joule heating power per unit area (see Eqs. (11)–(16)) for each magnetospheric configuration. The line code indicates the form of energy dissipation (thick solid curve shows total power). Total power is the sum of the magnetospheric and atmospheric powers and atmospheric power is the sum of Joule heating and ion drag powers. Integrating the power per unit area over the model hemisphere gives us the global powers for each of these mechanisms, shown in Fig. 8.

Fig. 7j–l exhibits peaks in power per unit area just equatorward of the interface between regions III and II due to the large ionospheric current associated with the breakdown in corotation of the magnetodisc (region III). Most of the energy dissipated in region III accelerates the magnetospheric plasma towards corotation. This magnetospheric power dominance diminishes for the expanded magnetosphere, in which more power is dissipated in the atmosphere via Joule heating and ion drag. Region II is dominated by these atmospheric power terms in cases B and C whilst the same region in case A is still noticeably magnetospheric power-dominated. Atmospheric power is the major form of energy dissipation in region I. The atmospheric power dominance in regions II and I is mainly due to the low assumed values for magnetospheric angular velocity Ω_M (see Fig. 2). The difference $(\Omega_T-\Omega_M)$ is largest in these regions, which produces relatively large ionospheric Pedersen currents and atmospheric power. The low value of Ω_M produces a magnetospheric power that remains low compared to other regions. Note that relative amounts of energy provided to the atmosphere and magnetosphere on any flux shell depends on the difference $(\Omega_T-\Omega_M)$ through Eqs. (12)–(14). They are equal when $\Omega_M=0.5\,\Omega_J$.

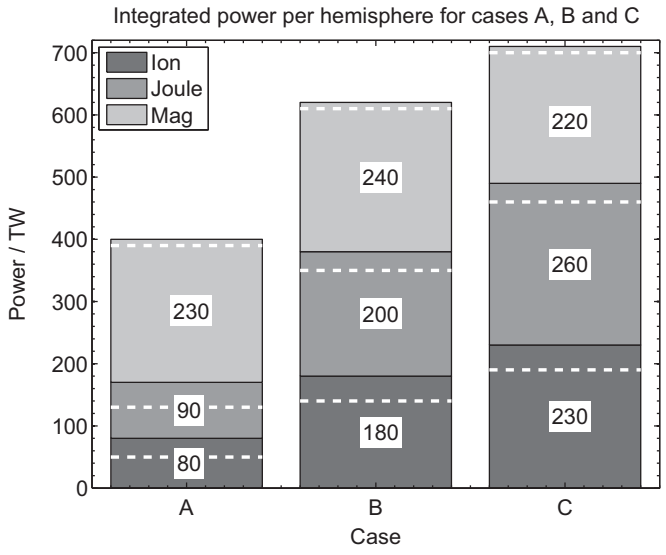

Fig. 8. Integrated ionospheric powers per hemisphere for cases A–C are represented in this figure. Ion drag is represented by dark grey bars, Joule heating by grey bars and magnetospheric power by light grey bars. The white dashed line shows the division in powers between closed and open field line regions. Powers in the closed field regions lie below the dashed white line whilst powers in the open field regions lie above it. Total power dissipated for each mechanism (in TW) is printed on its respective colour bar.

These figures suggest that as Jupiter's magnetosphere is compressed a higher proportion of the total power of planetary rotation (in the steady state) is transferred to the magnetosphere via the magnetic field, and by contrast, as the magnetosphere is expanded more heat is dissipated in the atmosphere.

Fig. 8 shows the integrated ion drag (dark grey), Joule heating (grey) and magnetospheric (light grey) power per hemisphere for each case and how these powers are distributed in the open and closed field line regions. Powers in the closed field regions lie below the dashed white line whilst powers in the open field regions lie above it. Integrated powers within region I remain essentially unchanged for both atmospheric (ion drag plus Joule heating) and magnetospheric mechanisms due to the assumed constant value of the magnetospheric angular velocity for all cases. Atmospheric power increases significantly with magnetospheric size, by a factor of $\sim$3 from case A to C. Magnetospheric power shows a slight decrease between cases A and C and is a maximum in case B. Magnetospheric power is proportional to the torque, which increases with magnetospheric expansion, and the magnetospheric angular velocity which decreases with expansion. One would thus expect that, given a large enough range of magnetospheric sizes, the magnetospheric power would display a non-monotonic profile that is 'modulated' by the difference between the angular velocity of the neutral thermosphere and plasmadisc.

We now compare our integrated powers per hemisphere with those calculated by Cowley et al. (2007) to take into account how using a two-dimensional model of Jupiter's thermosphere changes previous theoretical power estimates. We only compare cases A and B with the 'intermediate' and 'baseline' cases from Cowley et al. (2007) respectively as they have comparable magnetodisc radii. The total integrated magnetospheric powers per hemisphere are comparable in magnitude; 'intermediate' and 'baseline' cases in Cowley et al. (2007) are $\sim$85% those of our cases A and B. The difference between atmospheric powers is greater, since this study uses a detailed thermospheric model. In region I, cases A and B have atmospheric powers $\sim$35% of Cowley et al. (2007)'s 'intermediate' and 'baseline' cases. In regions III and II (closed field) the atmospheric powers in Cowley et al. (2007) are $\sim$70–80% those in cases A and B. Thus, within the closed field region of cases A and B, the inclusion of a detailed thermospheric flow model has led to more energy transferred from the thermosphere to the magnetosphere for accelerating the magnetospheric plasma and more heat dissipated within the thermosphere via Joule heating and ion drag.

4. Effect of outer boundary conditions

The results for case A exhibit a relatively large peak for the Pedersen conductivity and FAC density just equatorward of the boundary between regions III and II (Fig. 5). Previous studies such as Southwood and Kivelson (2001) suggest that such peaks for compressed magnetospheres should be smaller in magnitude than those for more expanded magnetospheres. This is in contrast to what we observe in Section 3. If the radial current at the region III/II boundary, $I_{\rho\infty}$ is larger than realistic values for a compressed magnetosphere, large FACs would develop in the poleward part of region III to satisfy the $I_{\rho\infty}$ boundary condition. In this section we present model outputs with smaller values of $I_{\rho\infty}$. We select illustrative $I_{\rho\infty}$ values for each case which minimise the variance in

the current profiles throughout regions III and II. Decreasing $I_{\rho\infty}$ decreases current gradients in the well constrained Ω_M model for region III and allows for a smoother transition to region II, whose Ω_M profile is poorly constrained (due to paucity of observations).

4.1. Outer boundary conditions for a compressed magnetosphere

To commence this part of our study, we ran case A but with $I_{\rho\infty}=45$ MA, to see whether any significant changes would arise in the currents at the region III/II boundary. These results are shown in Fig. 9, where blue and red lines represent cases A_{100} and A_{45} respectively (subscript denotes the value of $I_{\rho\infty}$).

4.1.1. Comparison of angular velocities and currents for case A

In this section we compare angular velocities and current-related parameters for cases A_{45} and A_{100} (case A in Section 3). The differences between these cases essentially lie within 72–78° latitude and so our subsequent discussions will focus on this range.

Fig. 9a shows the influence of $I_{\rho\infty}$ on the Ω_M and Ω_T values. Case A_{100} with the higher $I_{\rho\infty}$ value also has a higher torque on the disc plasma, which results in a smaller difference $\Omega_T-\Omega_M$ near the disc boundary (74–75°). Equatorward of 74°, the Ω_T and Ω_M profiles are very similar for both cases. The outer disc region 74–75° thus develops a strong FAC in case A_{100} in order to satisfy the higher $I_{\rho\infty}$ imposed.

Due to the smaller values of Ω_M and radial current for case A_{45}, Pedersen conductivity values (Fig. 9b) are significantly smaller near the region III/II boundary compared to case A_{100}. The different gradients in Ω_M and Ω_T for case A_{45} cause a slight equatorward shift in the conductivity peak compared to A_{100}. The 'slippage' parameter for A_{45} in Fig. 9c differs only slightly from that of case A_{100} due to its smaller $\Omega_T-\Omega_M$ differences.

The azimuthally integrated radial, Pedersen and FACs for cases A_{45} (red line) and A_{100} (blue line) are shown in Fig. 9d–f respectively. The other labels are the same as in Fig. 4. For A_{100} the magnetosphere near-rigidly corotates with Ω_J throughout regions IV and most of III (Nichols and Cowley, 2004). The A_{45} radial current profile resembles those for expanded cases, due to the magnetosphere sub-corotating to a greater degree (see Fig. 9a). The Pedersen current for case A_{45} has a smooth, almost linear transition across and through regions III and II as opposed to the abrupt cutoff at the region III/II boundary in A_{100}. The A_{45} profile quantitatively resembles Pedersen currents for expanded cases and those by Cowley et al. (2007). For A_{45}, FAC profiles are similar to those for A_{100} with the exception that the magnitude of the peaks just equatorward of the region III/II boundary and the trough are significantly smaller. For lower $I_{\rho\infty}$ values, then, the main auroral

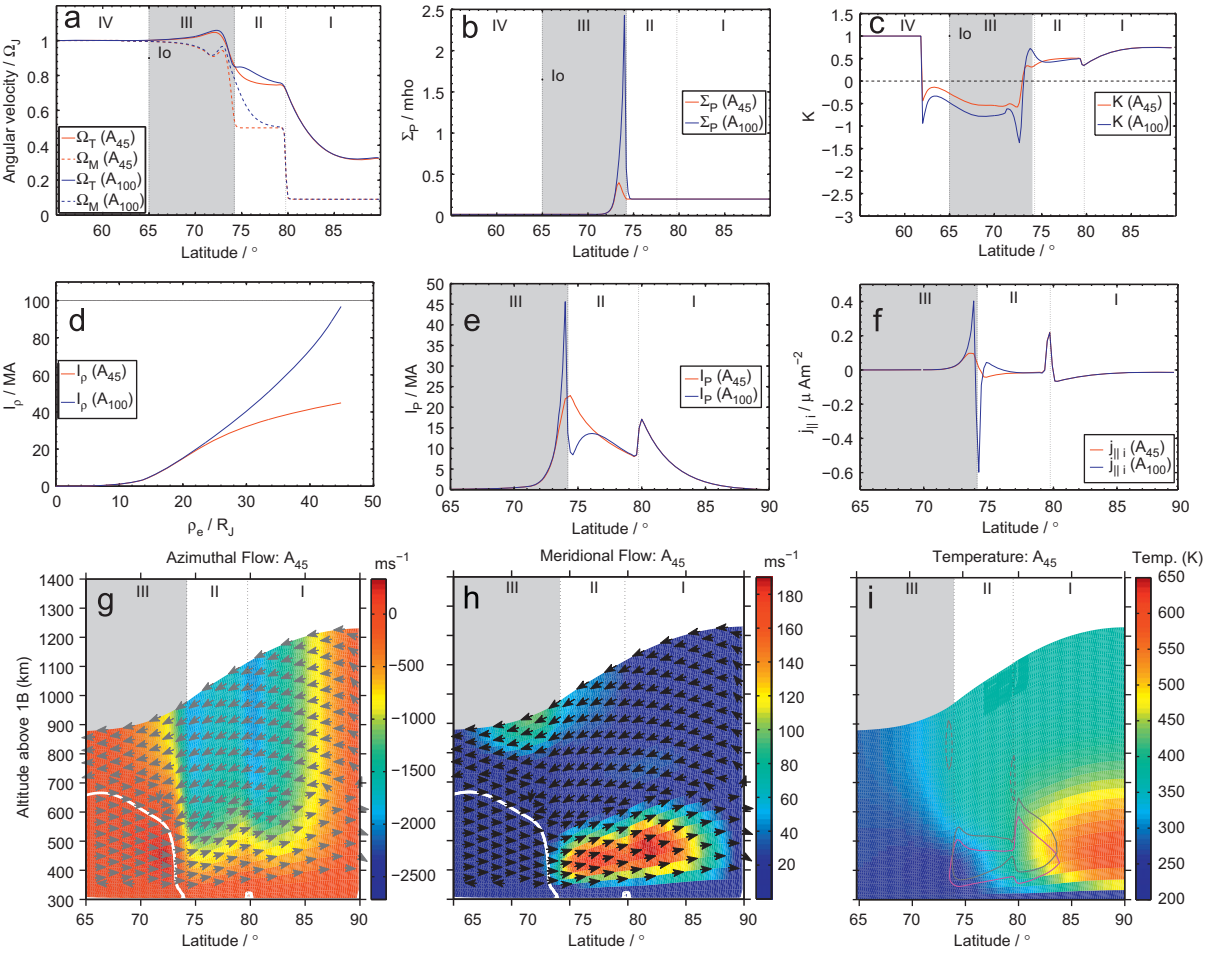

Fig. 9. (a)–(f) show thermospheric and magnetospheric angular velocities, height-integrated Pedersen conductivity, 'slippage' parameter, azimuthally integrated radial current, azimuthally integrated Pedersen current and FAC density respectively for case A with $I_{\rho\infty}=45$ MA (A_{45}) represented by red lines and case A with $I_{\rho\infty}=100$ MA (A_{100}) represented by blue lines. Note that case A_{100} is the same as case A in Section 3. For (a) the solid lines represent the thermospheric angular velocity and the dashed lines represent the magnetospheric angular velocity. Magnetospheric regions (region III is shaded) are labelled and separated by dotted black lines. (g)–(i) show this thermospheric azimuthal velocity, meridional velocity and temperature distributions in the high latitude region for case A_{45}. Arrows, contours and colour bars are the same as in Fig. 7.

oval would be significantly dimmer, and possibly more similar to the putatively weak auroral signature at the region I/II boundary.

4.1.2. Thermospheric distributions for case A

Here we discuss the changes in azimuthal and meridional velocity as well as the temperature distribution, which arise from setting $I_{\rho\infty} = 45$ MA for case A. All conventions and colours in Fig. 9g and h are the same as those in Fig. 7.

Fig. 9g and h shows the distribution of azimuthal and meridional velocities across the high latitude region for case A_{45}. In A_{100} (Fig. 7a) there is a large sub-corotational jet in regions II and I with the strongest degree of sub-corotation just poleward of the region II/I boundary. In A_{45}, the large sub-corotating jet now has two regions of strong sub-corotation, the new one being just poleward of the region III/II boundary. These two strong sub-corotational jets within the larger jet are evident in Fig. 9a at the region boundaries (dotted black lines), where there are large changes in magnetospheric angular velocity. Meridional velocities for case A_{45} follow the same trend as in A_{100} (Fig. 7d) where there is a poleward flow at low altitudes and an opposite flow at high altitudes. The main difference between the meridional flows is that localised accelerated flows (high altitude in region III and low altitude in regions II and I) have larger velocities in case A_{45} due to larger advection terms.

Fig. 9i shows the temperature distribution for case A_{45}. Comparing this with case A_{100} (Fig. 7g) indicates that energy input via Joule heating (magenta contours) and ion drag (solid grey contours) is greater in A_{45}. The larger energy input, predominantly in region II, is caused by larger shear between thermospheric and magnetospheric angular velocities. This leads to a slight increase in thermospheric temperature ($\sim 6\%$) most evident in region I, the polar 'hotspot' into which auroral heat energy is transported by meridional winds.

4.2. Outer boundary conditions for the baseline magnetosphere

For our baseline case, case B, the smallest variance in current profiles occurred with $I_{\rho\infty} = 68$ MA. We compare this case B_{68} with the original B_{100} case in Fig. 10.

4.2.1. Comparison of angular velocities and currents for case B

As for the compressed magnetosphere, we compare angular velocities and current-related parameters of the B_{68} and B_{100} models in the 72–75° latitude range where significant differences arise. Fig. 10a compares the variation of magnetospheric and thermospheric angular velocities for cases B_{68} and B_{100}. In region III, both the magnetosphere and thermosphere for B_{68} are slightly sub-corotating compared to the B_{100}. The Pedersen conductivity and 'slippage' parameter for B_{68} also have similar profiles, but with smaller magnitudes in region III, to those for B_{100}. These

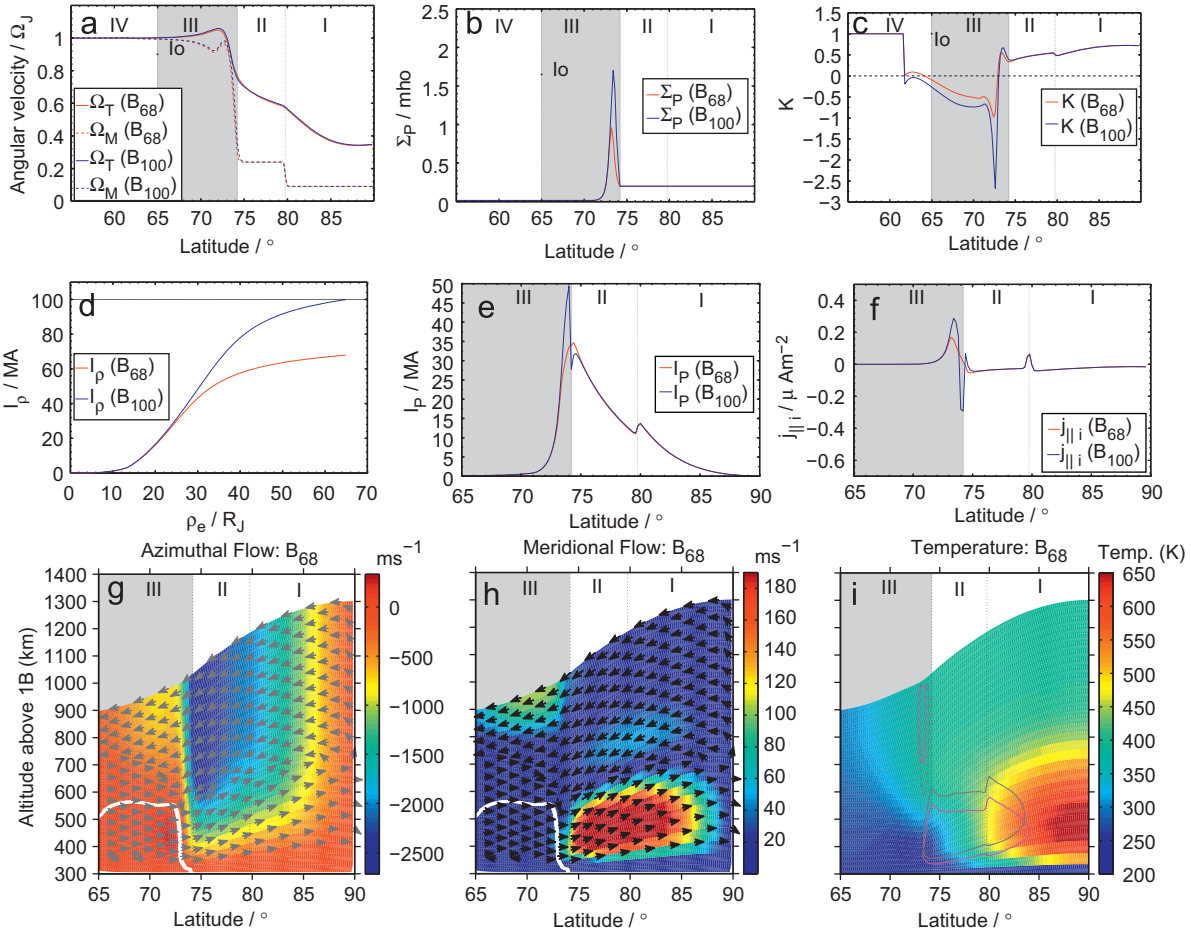

Fig. 10. (a)–(f) show thermospheric and magnetospheric angular velocities, height-integrated Pedersen conductivity, 'slippage' parameter, azimuthally integrated radial current, azimuthally integrated Pedersen current and FAC density respectively for case B with $I_{\rho\infty} = 68$ MA (B_{68}) represented by red lines and case B with $I_{\rho\infty} = 100$ MA (B_{100}) represented by blue lines. Note that case B_{100} is the same as case B in Section 3. For (a) the solid lines represent the thermospheric angular velocity and the dashed lines represent the magnetospheric angular velocity. Magnetospheric regions (region III is shaded) are labelled and separated by dotted black lines. (g)–(i) show this thermospheric azimuthal velocity, meridional velocity and temperature distribution in the high latitude region for case B_{68}. Arrows, contours and colour bars are the same as in Fig. 7.

minor differences are caused by smaller thermospheric and magnetospheric angular velocities in region III.

Fig. 10d and e shows azimuthally integrated radial and Pedersen currents. The corresponding FAC density as a function of latitude is shown in Fig. 10f. The radial current profile is smaller in magnitude than that of B_{100}. The B_{68} Pedersen current has a single small peak at the region III/II boundary in contrast with the sharp peak in B_{100}. The FAC density has a smaller, slightly broader peak in region III, suggesting a low intensity auroral oval compared to the B_{100} case. The absence of strong downward FAC for B_{68} also suggests that the method used to join the region III currents with the region II currents could produce artefacts for relatively large values of $I_{\rho\infty}$.

As with case A, the fine structure around the boundary between the middle and outer magnetosphere in Fig. 10a–f has been removed by decreasing the value of $I_{\rho\infty}$ from 100 MA to 68 MA for our baseline case.

4.2.2. Thermospheric distributions for case B

Here we discuss the minor changes in Jupiter's thermospheric flows and temperature distribution made by changing the radial current boundary condition value for our baseline case. All conventions and colours are the same as those in Fig. 7.

The azimuthal velocity in the high latitude region is shown in Fig. 10g. We expect a slight increase in sub-corotation throughout region III (see Fig. 10a) compared to B_{100}. This is evident by comparing Fig. 10g with Fig. 7a where we can see that the region of super-corotation (dark red) has diminished for B_{68}. The meridional velocity distribution is shown in Fig. 10h. The high altitude localised accelerated flow in region III is slightly faster than in case B_{100} because the pressure gradient and advection terms are 27–40% larger in this region of B_{68}. This would lead to a minimal temperature increase $\sim 3\%$, most notably in regions II and I (see Fig. 10i).

4.3. Outer boundary conditions for an expanded magnetosphere

For our expanded configuration, we found that $I_{\rho\infty} = 80$ MA gave a smooth profile (least variance in FAC density). This change in $I_{\rho\infty}$ produced corresponding changes in model outputs, which are far less significant than those from our compressed case. Both magnetospheric and thermospheric angular velocities in case C_{80} have slightly smaller magnitudes in the magnetodisc region when compared to C_{100}. The current profiles calculated by setting $I_{\rho\infty} = 80$ MA produced currents strongly resembling those for case B_{68}. Peak values for currents at the region III/II boundary are ~ 70–80% of those in case C_{100}. Thermospheric flows for C_{80} differ slightly from C_{100}, most significantly in the larger degree of sub-corotation in C_{80}. The 'hotspot' in the polar region is $\sim 2\%$ hotter than in case C_{100} because of faster poleward flows transporting heat more efficiently. These faster flows are due to stronger advection in case C_{80} producing stronger acceleration compared to C_{100}.

4.4. Effect of outer boundary conditions on ionospheric powers

In this section, we examine figures for ionospheric power per unit area and their respective integrated power per hemisphere for cases A_{45}, B_{68} and C_{80}.

The power per unit area for case A_{45} in the high latitude region is shown in Fig. 11a. Line conventions and labels are the same as those in Fig. 7j–l. Powers per unit area (in Fig. 11a) are integrated

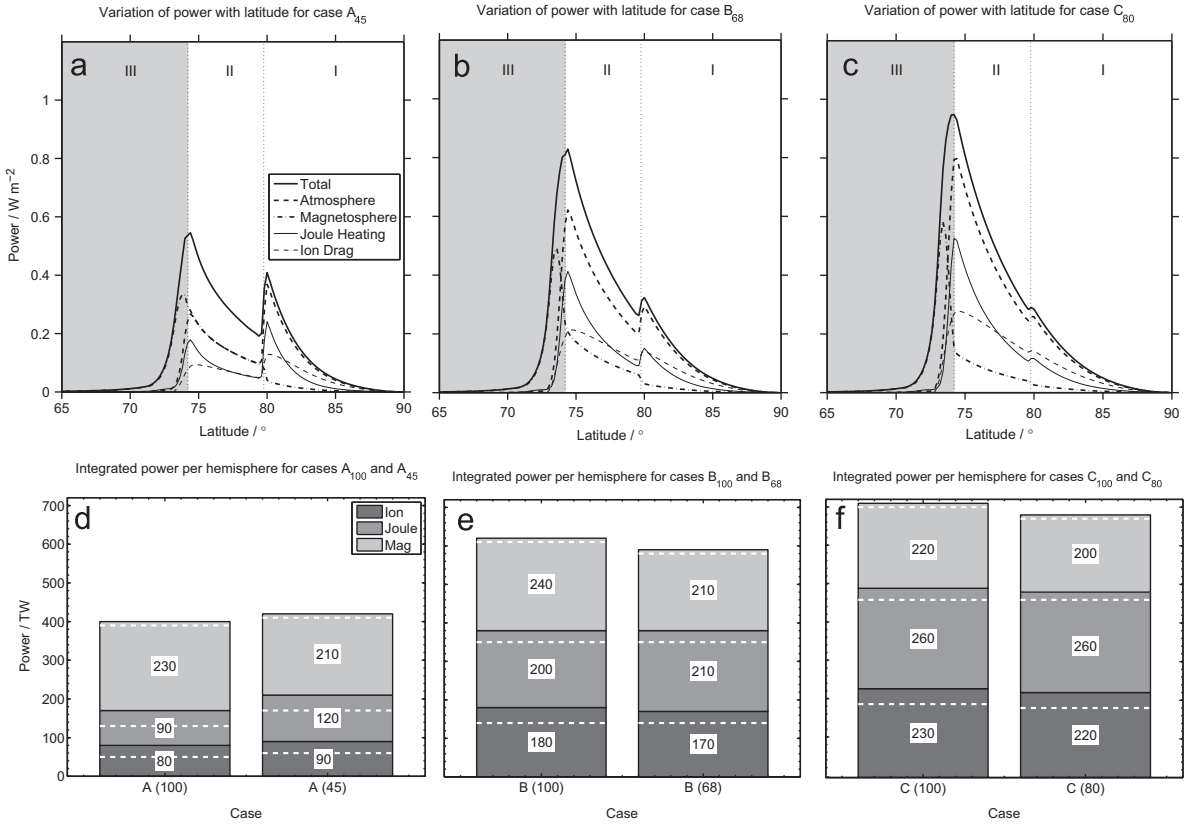

Fig. 11. (a)–(c) show ionospheric powers per unit area in the high latitude region for cases A_{45}, B_{68} and C_{80} respectively. Total power per unit area is represented by the thick solid line, magnetospheric power by the thick dot-dashed line, atmospheric power by the thick dashed line, Joule heating by the thin solid line and ion drag power by the thin dashed line. Magnetospheric regions are labelled and separated by dotted black lines. (d)–(f) show integrated powers per hemisphere for cases A_{45}, B_{68} and C_{80} respectively. Ion drag, Joule heating and magnetospheric powers are indicated by dark grey, grey and light grey bars. Powers in the closed field line regions lie below the white dashed line whilst powers in the open field regions lie above it. Total power dissipated for each mechanism (in TW) is printed on its respective colour bar.

over each hemisphere and are shown in Fig. 11d. The transition between regions III and II is the most interesting for comparison; A_{100} has a large prominent peak in magnetospheric power whereas A_{45} has a significantly reduced peak due to smaller values of Ω_M. In region II $\Omega_M \sim 0.5\Omega_J$ (see Fig. 9a) implying that magnetospheric and atmospheric power in this region are equal. Joule heating and ion drag are thus increased in A_{45} compared to A_{100} to meet the above requirement. These results suggest that smaller $I_{\rho\infty}$ values will generally dissipate more heat in the atmosphere but less efficiently maintain corotation in the magnetosphere.

For cases B_{68} and C_{80} the power per unit area and integrated powers per hemisphere are shown in Fig. 11b, c and e,f respectively. In comparing these two cases with B_{100} and C_{100} we find only small differences in atmospheric powers (Joule heating and ion drag), predominantly at the region III/II boundary where there are two peaks with a small trough in between. The integrated atmospheric powers per hemisphere thus remain relatively uniform with the changes in $I_{\rho\infty}$ specified for all baseline (B_{68} and B_{100}) and expanded (C_{80} and C_{100}) cases. The magnetospheric power per unit area for B_{68} and C_{80} has significantly smaller magnitudes in region III compared to their $I_{\rho\infty} = 100$ MA counterparts. Therefore, for these configurations of the magnetosphere, decreasing the value of $I_{\rho\infty}$ decreases the efficiency with which the atmosphere can accelerate the magnetosphere towards corotation, but has no significant effect on atmospheric powers.

5. Conclusion

In this study, we have expanded the model of SA09 and described the effects of different solar wind dynamic pressures on the coupled ionosphere–magnetosphere system at Jupiter. We constructed three typical magnetospheric profiles (see Table 1), compressed, baseline (average) and expanded. These were then coupled to our global two-dimensional thermospheric model (Smith and Aylward, 2008) and a global conductivity model of the ionosphere (GG). This allowed for a comparison with results from SA09, but also provided a first quantitative investigation of how ionospheric, thermospheric and magnetospheric parameters were affected by differing solar wind conditions.

Our results confirm many results from previous studies such as those of Southwood and Kivelson (2001), Cowley and Bunce (2003a) and Cowley et al. (2007). We see an increase (resp. decrease) in thermospheric and magnetospheric angular velocities for compressed (resp. expanded) magnetospheres relative to our baseline. The thermosphere super-corotates just equatorward of the middle/outer magnetosphere boundary similar to SA09. We solve for Ω_M self-consistently in the magnetodisc in all cases using the equations of disc dynamics. The Ω_M value in the outer magnetosphere is a constant, dependent on disc radius, i.e. solar wind pressure (Cowley et al., 2005). Magnetospheric angular velocities in the polar cap are also fixed at a set fraction ($\sim 10\%$) of rigid corotation (Ω_J) (Isbell et al., 1984). We also found that the coupling currents showed an increase ($\sim 20\%$) in intensity when going from an average to a more expanded magnetosphere and a decrease ($\sim 40\%$) when going from average to compressed.

Our thermospheric model was used to simulate azimuthal and meridional neutral velocities. We see super-corotation in the azimuthal flows equatorward of the edge of the magnetodisc flux shells. There lies a strong sub-corotational jet at mid to upper altitudes in the mapped ionospheric locations of the outer magnetosphere and polar cap. The spatial size of the strong sub-corotation region increases with increased magnetospheric size due to the weaker magnetic field strength in expanded magnetospheres; thus the transfer of angular momentum is less effective at maintaining corotation. Angular momentum is transferred from the thermosphere to the magnetosphere, in order to accelerate the latter towards corotation. If the thermosphere itself is significantly sub-corotating, then there is a lower 'reservoir' of available angular momentum that can be transferred. This results in a decreased plasma angular velocity in these outer regions of the magnetosphere. We see a meridional flow directed polewards at low altitudes and equatorwards at high altitudes. From the poleward edge of the magnetodisc to the centre of the polar cap, a region of accelerated poleward flow exists whose velocity magnitude increases from a compressed to an expanded magnetosphere. This occurs because there is a force imbalance in this region that increases advection of momentum in expanded magnetospheres. Advection restores balance which results in the acceleration discussed above. This accelerated flow produces a 'hotspot' in the polar cap, with a maximum temperature increase of ~ 130 K from compressed to expanded magnetosphere. The size of the 'hotspot' also increases with an expanding magnetosphere. We find that the outer magnetosphere and polar cap are most strongly heated by Joule heating and ion drag. This heat is then distributed across the polar region via advection rather than viscous transport, whilst more equatorial regions are significantly cooled. This aspect of thermospheric flow is consistent with those presented in SA09. These results also suggest that accurate measurements of ionospheric temperature in the polar region could potentially be used to probe magnetospheric conditions.

We also showed that the power dissipated in the upper atmosphere (consisting of both Joule heating and ion drag) increases with an expanded magnetospheric configuration. The power used to accelerate the magnetospheric plasma initially increases as we expand the magnetosphere from compressed to average configurations, but then decreases with an expansion from average to expanded. This suggests that power used to accelerate the magnetosphere has a 'local' maximum for a magnetosphere size somewhere between a compressed and expanded configuration. The total power extracted from planetary rotation is the net sum of the atmospheric and magnetospheric powers and this is positively correlated with magnetosphere size. Comparing our compressed and average magnetospheres with the 'intermediate' and 'baseline' cases in Cowley et al. (2007), we showed that the use of a two-dimensional thermosphere model results in the transfer of $\sim 20\%$ more energy from the thermosphere to the magnetosphere in order to accelerate the plasma in the magnetodisc. Using our more realistic model of thermospheric flow also produced increased dissipation of energy in the thermosphere via Joule heating and ion drag than the cases presented by Cowley et al. (2007).

We have shown that our original compressed case has some unusual current density features due to a relatively high value for the radial current at the outer disc boundary. In order to confirm this we decreased the boundary value of $I_{\rho\infty}$ for each case in order to produce alternative models with minimum variance in their FAC profiles. This led to the selection of $I_{\rho\infty}$ of 45 MA, 68 MA and 80 MA for the compressed, average and expanded cases respectively.

Decreasing the radial current $I_{\rho\infty}$ at the boundary between the middle and outer magnetospheres resulted in all magnetosphere–ionosphere coupling currents being reduced in accordance with the new value of $I_{\rho\infty}$. This is expected under the assumption of current continuity. The main differences between cases with large and reduced radial currents lies mainly within the magnetodisc. For the FAC density, changes related to $I_{\rho\infty}$ were also significant throughout the outer magnetosphere. Thermospheric and magnetospheric angular velocities changed only slightly for the baseline and expanded case but much more substantially for our compressed case. For azimuthal flows we found that decreasing $I_{\rho\infty}$ also generally increased the level of sub-corotation throughout high latitudes. For meridional flows we found slight increases

in localised regions of accelerated flow, most evident in the alternate compressed case. We also found that the polar region becomes slightly warmer with a decrease in $I_{\rho\infty}$; peak temperatures for the alternative configurations increasing relative to their $I_{\rho\infty}=100$ MA counterparts. The total integrated powers increased with decreasing $I_{\rho\infty}$ for our compressed case, but decreased for our baseline and expanded cases. The integrated magnetospheric power for all cases decreased along with $I_{\rho\infty}$, whilst atmospheric power increased by $\sim 20\%$ for the alternate compressed case but remained almost equal for our baseline and expanded cases. Thus, it seems that decreasing the boundary radial current $I_{\rho\infty}$ effectively decreases the 'ability' of the thermosphere to transfer angular momentum to the magnetosphere. This behaviour, as expected decreases the intensity of auroral emissions and produces a slightly warmer polar region.

Our calculations suggest that main oval auroral emissions and brightness for an expanded magnetosphere would generally be greater than that of a compressed one. The detailed structure of the FAC density profile in the magnetodisc is most sensitive to the value of $I_{\rho\infty}$ for the compressed case. Compressed magnetospheres in the steady state have larger field strength than expanded ones and are more efficient at maintaining the corotating magnetodisc plasma at larger distances. This leads to a smaller shear in angular velocity between the magnetosphere and thermosphere and, consequently, smaller thermospheric temperatures. As a result, auroral emission is brightest for the most expanded magnetospheric systems. We also saw that auroral emissions would increase at the boundary between the outer magnetosphere and the polar region with magnetospheric compression due to the large change in plasma angular velocity at this boundary. Better observational constraints of Ω_M are required to confirm this prediction.

This aspect warrants further investigation since we have not attempted to model the change in polar cap angular velocity with solar wind dynamic pressure. Furthermore, the caveat with these predictions is that the system is in a steady-state (where there is no explicit time dependence of the model outputs). We thus view this study as an initial step towards developing a model to study the transient effects of rapid changes in the solar wind dynamic pressure. Results of such studies could provide further insights to the 'energy crisis' at Jupiter (SA09), and the physical origin of transient auroral features.

Finally, the results presented in this study contribute to a larger set of theoretical investigations which have provided useful quantitative predictions of how the Jovian aurorae would respond to changes in solar wind dynamic pressure. Such results are useful for interpreting auroral observations, and for making more extensive use of such data as remote diagnostics of the physical state of the Jovian magnetosphere.

Acknowledgement

JNY was supported by an STFC studentship award. The authors express their gratitude to Chris Smith who developed the coupled model used herein. The authors acknowledge support of the STFC funded Miracle Consortium (part of the DiRAC facility) in providing access to computational resources. Finally, the authors would like to thank the referees for their useful suggestions throughout the peer review process.

References

Bagenal, F., Sullivan, J.D., 1981. Direct plasma measurements in the Io torus and inner magnetosphere of Jupiter. Journal of Geophysical Research 86, 8447–8466.

Clarke, J.T., Ben Jaffel, L., Gérard, J., 1998. Hubble space telescope imaging of Jupiter's UV aurora during the Galileo orbiter mission. Journal of Geophysical Research 103, 20217–20236.

Clarke, J.T., Grodent, D., Cowley, S.W.H., Bunce, E.J., Zarka, P., Connerney, J.E.P., Satoh, T., 2004. Jupiter's aurora. Jupiter: The Planet, Satellites and Magnetosphere, 639–670.

Connerney, J.E.P., Acuña, M.H., Ness, N.F., Satoh, T., 1998. New models of Jupiter's magnetic field constrained by the Io flux tube footprint. Journal of Geophysical Research 103, 11929–11940.

Connerney, J.E.P., Acuna, M.H., Ness, N.F., 1981. Modeling the Jovian current sheet and inner magnetosphere. Journal of Geophysical Research 86, 8370–8384.

Cowley, S.W.H., Alexeev, I.I., Belenkaya, E.S., Bunce, E.J., Cottis, C.E., Kalegaev, V.V., Nichols, J.D., Prangé, R., Wilson, F.J., 2005. A simple axisymmetric model of magnetosphere–ionosphere coupling currents in Jupiter's polar ionosphere. Journal of Geophysical Research 110, 11209–11226.

Cowley, S.W.H., Bunce, E.J., 2001. Origin of the main auroral oval in Jupiter's coupled magnetosphere–ionosphere system. Planetary and Space Science 49, 1067–1088.

Cowley, S.W.H., Bunce, E.J., 2003a. Modulation of Jovian middle magnetosphere currents and auroral precipitation by solar wind-induced compressions and expansions of the magnetosphere: initial response and steady state. Planetary and Space Science 51, 31–56.

Cowley, S.W.H., Bunce, E.J., 2003b. Modulation of Jupiter's main auroral oval emissions by solar wind induced expansions and compressions of the magnetosphere. Planetary and Space Science 51, 57–79.

Cowley, S.W.H., Nichols, J.D., Andrews, D.J., 2007. Modulation of Jupiter's plasma flow, polar currents, and auroral precipitation by solar wind-induced compressions and expansions of the magnetosphere: a simple theoretical model. Annales Geophysicae 25, 1433–1463.

Drossart, P., Bezard, B., Atreya, S.K., Bishop, J., Waite Jr., J.H., Boice, D., 1993. Thermal profiles in the auroral regions of Jupiter. Journal of Geophysical Research 98, 18803–18811.

Grodent, D., Clarke, J.T., Kim, J., Waite, J.H., Cowley, S.W.H., 2003. Jupiter's main auroral oval observed with HST-STIS. Journal of Geophysical Research 108, 1389–1404.

Grodent, D., Gérard, J., 2001. A self-consistent model of the Jovian auroral thermal structure. Journal of Geophysical Research 106, 12933–12952.

Hill, T.W., 1979. Inertial limit on corotation. Journal of Geophysical Research 84, 6554–6558.

Hill, T.W., 2001. The Jovian auroral oval. Journal of Geophysical Research 106, 8101–8108.

Hill, T.W., Dessler, A.J., Goertz, C.K., 1983a. Magnetospheric models. In: Physics of the Jovian Magnetosphere, pp. 353–394.

Hill, T.W., Dessler, A.J., Rassbach, M.E., 1983b. Aurora on Uranus – A Faraday disc dynamo mechanism. Planetary and Space Science 31, 1187–1198.

Huang, T.S., Hill, T.W., 1989. Corotation lag of the Jovian atmosphere, ionosphere, and magnetosphere. Journal of Geophysical Research 94, 3761–3765.

Huddleston, D.E., Russell, C.T., Kivelson, M.G., Khurana, K.K., Bennett, L., 1998. Location and shape of the Jovian magnetopause and bow shock. Journal of Geophysical Research 103, 20075–20082.

Isbell, J., Dessler, A.J., Waite Jr., J.H., 1984. Magnetospheric energization by interaction between planetary spin and the solar wind. Journal of Geophysical Research 89, 10716–10722.

Joy, S.P., Kivelson, M.G., Walker, R.J., Khurana, K.K., Russell, C.T., Ogino, T., 2002. Probabilistic models of the Jovian magnetopause and bow shock locations. Journal of Geophysical Research 107, 1309–1325.

Khurana, K.K., 2001. Influence of solar wind on Jupiter's magnetosphere deduced from currents in the equatorial plane. Journal of Geophysical Research 106, 25999–26016.

Khurana, K.K., Kivelson, M.G., 1993. Inference of the angular velocity of plasma in the Jovian magnetosphere from the sweepback of magnetic field. Journal of Geophysical Research 98, 67–79.

Kivelson, M.G., Bagenal, F., Kurth, W.S., Neubauer, F.M., Paranicas, C., Saur, J., 2004. Magnetospheric interactions with satellites. Jupiter: The Planet, Satellites and Magnetosphere, 513–536.

Kivelson, M.G., Russell, C.T., 1995. Introduction to Space Physics. pp. 183–202.

McNutt Jr., R.L., Belcher, J.W., Sullivan, J.D., Bagenal, F., Bridge, H.S., 1979. Departure from rigid co-rotation of plasma in Jupiter's dayside magnetosphere. Nature 280, 803.

Miller, S., Stallard, T., Smith, C., et al., 2006. H3+: the driver of giant planet atmospheres. Philosophical Transactions Series A 364, 3121–3137.

Nichols, J., Cowley, S., 2004. Magnetosphere-ionosphere coupling currents in Jupiter's middle magnetosphere: effect of precipitation-induced enhancement of the ionospheric Pedersen conductivity. Annales Geophysicae 22, 1799–1827.

Pallier, L., Prangé, R., 2001. More about the structure of the high latitude Jovian aurorae. Planetary and Space Science 49, 1159–1173.

Pontius, D.H., 1995. Implications of variable mass loading in the Io torus: the Jovian flywheel. Journal of Geophysical Research 100, 19531–19540.

Pontius, D.H., 1997. Radial mass transport and rotational dynamics. Journal of Geophysical Research 102, 7137–7150.

Prangé, R., Rego, D., Pallier, L., Connerney, J., Zarka, P., Queinnec, J., 1998. Detailed study of FUV Jovian auroral features with the post-COSTAR HST faint object camera. Journal of Geophysical Research 103, 20195–20216.

Satoh, T., Connerney, J.E.P., Baron, R.L., 1996. Emission source model of Jupiter's H3+ aurorae: a generalized inverse analysis of images. Icarus 122, 1–23.

Smith, C.G.A., Aylward, A.D., 2008. Coupled rotational dynamics of Saturn's thermosphere and magnetosphere: a thermospheric modelling study. Annales Geophysicae 26, 1007–1027.

Smith, C.G.A., Aylward, A.D., 2009. Coupled rotational dynamics of Jupiter's thermosphere and magnetosphere. Annales Geophysicae 27, 199–230.
Smith, C.G.A., Aylward, A.D., Millward, G.H., Miller, S., Moore, L.E., 2007. An unexpected cooling effect in Saturn's upper atmosphere. Nature 445, 399–401.
Smith, C.G.A., Miller, S., Aylward, A.D., 2005. Magnetospheric energy inputs into the upper atmospheres of the giant planets. Annales Geophysicae 23, 1943–1947.
Southwood, D.J., Kivelson, M.G., 2001. A new perspective concerning the influence of the solar wind on the Jovian magnetosphere. Journal of Geophysical Research 106, 6123–6130.
Tao, C., Fujiwara, H., Kasaba, Y., 2009. Neutral wind control of the Jovian magnetosphere-ionosphere current system. Journal of Geophysical Research 114, 8307–8323.
Vasavada, A.R., Bouchez, A.H., Ingersoll, A.P., Little, B., Anger, C.D., 1999. The Galileo SSI Team, 1999. Jupiter's visible aurora and Io footprint. Journal of Geophysical Research 104, 27133–27142.
Vasyliunas, V.M., 1983. Plasma distribution and flow. In: Physics of the Jovian Magnetosphere, pp. 395–453.